Int J Earth Sci (Geol Rundsch) (2009) 98:551–569
DOI 10.1007/s00531-007-0268-x

ORIGINAL PAPER

Early Paleozoic tectonic evolution of the Chinese South Tianshan Orogen: constraints from SHRIMP zircon U–Pb geochronology and geochemistry of basaltic and dioritic rocks from Xiate, NW China

Qing Qian · Jun Gao · Reiner Klemd · Guoqi He · Biao Song · Dunyi Liu · Ronghua Xu

Received: 5 January 2007 / Accepted: 11 October 2007 / Published online: 13 November 2007

Abstract Traditionally the Chinese South Tianshan has been regarded as a late Paleozoic orogenic belt. However, little is known about the early Paleozoic tectonic architecture of the region. This paper presents the first evidence of Cambrian–Ordovician MORB-type basalts and adakitic diorites on the southern margin of the Yili plate in China. Basalts from Xiate in southwestern Tianshan show a typical transitional (T-) MORB and ferrobasalt composition, which indicate a formation at a propagating spreading ridge. The basalts give a weighted mean $^{206}Pb/^{238}U$ crystallization age of 516.3 ± 7.4 Ma by SHRIMP U–Pb zircon dating and have experienced contact metamorphism due to the intrusion of a dioritic pluton. The dioritic pluton has a weighted mean $^{206}Pb/^{238}U$ crystallization age of 470 ± 12 Ma and geochemical characteristics resembling that of adakitic rocks. The pluton is considered to have been formed by partial melting of garnet amphibolites from thickened lower crust in arc or continental collision settings. The basalts and diorites are considered to outline the eastern extension of the early Paleozoic suture zone, the Nikolaev Line, which stretches east–west for hundreds of kilometers between the Northern Tianshan and Central Tianshan terranes of Kyrgyzstan. Our findings substantiate that the Yili and Central Tianshan plates were separated by the early Paleozoic Terskey ocean. The Terskey ocean probably closed during the early stage of the late Ordovician (Lomize et al. in Geotectonics 31(6):463–482, 1997), resulting in the final amalgamation of the Yili and Central Tianshan plates. Consequently, an early Paleozoic suture zone is documented in the Chinese Tianshan region, which is most likely represented by the North Nalati fault.

Keywords South Tianshan · Early Paleozoic · MORB · Adakite · SHRIMP geochronology · Geochemistry

Introduction

The Paleozoic Tianshan orogen extends for ca. 2,500 km in the southernmost part of the Altaids (Sengör et al. 1993) and is dominated by subduction and collision (Coleman 1989; Windley et al. 1990; Allen et al. 1992; Gao et al. 1998). It was reactivated during the late Cenozoic due to the India–Eurasia collision and experienced intracontinental deformation, after being quiescent for the Mesozoic and much of the Cenozoic (Hendrix et al. 1994; Burtman et al. 1996; Sobel et al. 2006). The neotectonics, however, are grossly controlled by the Paleozoic structures, and two late Paleozoic suture zones, the North Tianshan and South Tianshan suture zones (Fig. 1), have been documented in the northern and southern Tianshan ranges (Windley et al. 1990). The suture zones divide the Chinese part of the Tianshan and adjacent area into three tectonic units: the

Q. Qian (✉) · J. Gao · R. Xu
Key Laboratory of Mineral Resources, Institute of Geology and Geophysics, Chinese Academy of Sciences, P.O. BOX 9825, Beijing 100029, China
e-mail: qianqing@mail.igcas.ac.cn

R. Klemd
Mineralogisches Institut, Universität Würzburg, Am Hubland, Würzburg 97074, Germany

G. He
School of Earth and Space Sciences, Peking University, Beijing 100871, China

B. Song · D. Liu
Beijing SHRIMP Center, and Institute of Geology, Chinese Academy of Geological Sciences, Beijing 100081, China

Junggar, the Yili–Central Tianshan and the Tarim plates from north to south (Windley et al. 1990; Allen et al. 1992; Gao et al. 1998; Shu et al. 2004). Two Paleozoic oceans, the Paleo-Junggar and the South Tianshan oceans, are represented by the North Tianshan and the South Tianshan suture zones, respectively. The Paleo-Junggar ocean was subducted southward beneath the Yili–Central Tianshan plate and closed in early or late Carboniferous (Coleman 1989; Windley et al. 1990; Allen et al. 1992; Gao et al. 1998; Wang et al. 2006). The South Tianshan ocean (STO) was subducted northward beneath the Yili–Central Tianshan plate and it is generally accepted to have closed during the early Carboniferous (Windley et al. 1990; Allen et al. 1992; Carroll et al. 1995; Gao et al. 1998, 2006).

The early Paleozoic Karatau–Terskey suture zone, which is also known as the Nikolaev Line, separates the North and Central Tianshan plates in Kyrgyzstan (Fig. 1). This suture marks the position of the Terskey ocean, which closed in the early stage of the late Ordovician (Lomize et al. 1997). Remnants of the ocean are represented by a belt of Cambrian–Ordovician ophiolites and arc-type magmatic rocks on the southern margin of the Kyrgyzstan Northern Tianshan. Outcrops of the ophiolites and arc rocks disappear in the glacial region of the Hantengri Peak. Based on regional tectonic analysis, He and Li (2000) and He et al. (2001) proposed that the Terskey ophiolitic belt extends into the Chinese South Tianshan region, while Li and Li (1997) suggested that the Nikolaev Line probably is connected with the North Nalati fault (NNF). However, no substantial evidence of coeval ophiolites and arc-type rocks has been found in the Chinese South Tianshan, and the NNF is considered to be a secondary fault of the South Tianshan suture zone (STSZ) rather than an independent suture zone (Li and Li 1997). Records of the Terskey ocean in the Chinese Tianshan may largely have been destroyed by later geological events, such as Cenozoic intracontinental deformation and Paleozoic magmatism caused by the subduction of the STO. Alternatively, the Terskey ocean may originally have been confined to the Kyrgyzstan Northern Tianshan range and did not develop in the Chinese Tianshan. Unraveling the enigma is vital for the reconstruction of the early Paleozoic tectonic architecture of the Tianshan orogen and, thus, for the tectonic framework of Paleozoic Central Asia. This paper reports the results of our recent geochemical and geochronological studies of Cambrian basalts and Ordovician diorites, which occur along the NNF between the Yili and Central Tianshan plates in western China. A tectonic model is then proposed for the early Paleozoic tectonic evolution of the Chinese South Tianshan orogen.

Geologic background and fieldwork

The study area is located on the south margin of the Yili plate, to the north of the NNF and about 25–35 km north of the STSZ (Figs. 1, 2). The STSZ marks the closure of the STO in late Paleozoic and separates the Tarim plate from the Yili–Central Tianshan plate (Allen et al. 1992; Carroll et al. 1995; Gao et al. 1998). The NNF is connected to the

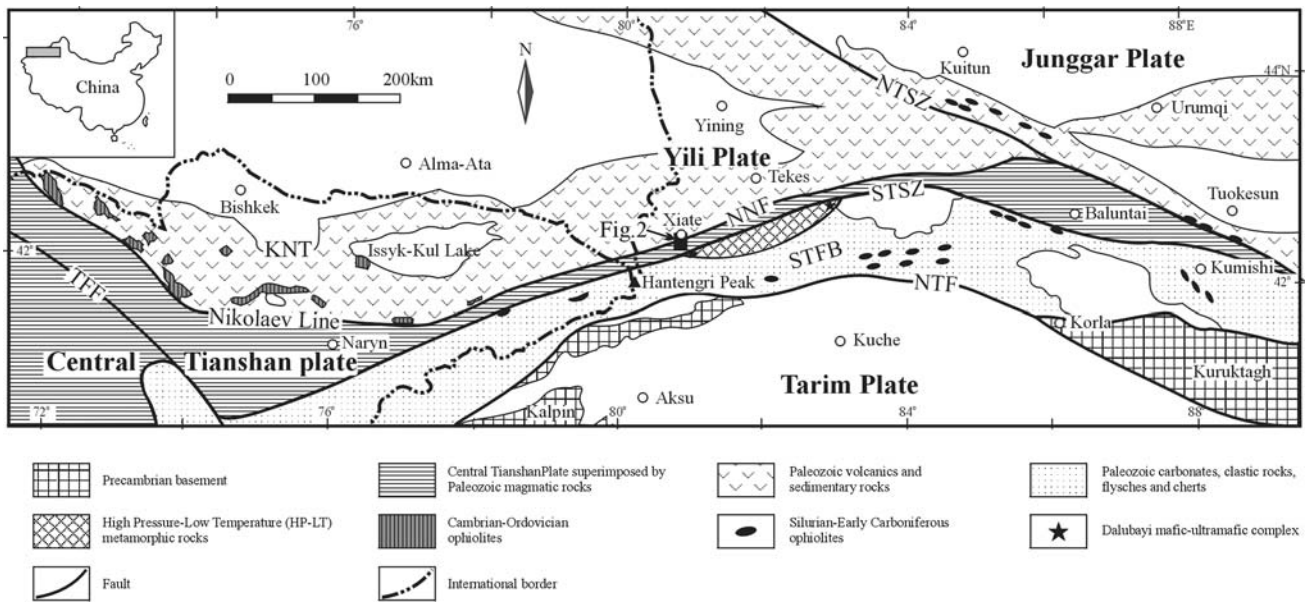

Fig. 1 Simplified geological map of the Bishkek-Urumqi region of the Tianshan range, modified after Gao et al. (1998) and Lomize et al. (1997). *KNT* Kyrgyzstan Northern Tianshan, *NNF* North Nalati Fault, *NTF* North Tarim fault, *NTSZ* North Tianshan suture zone, *STFB* South Tianshan fold belt, *STSZ* South Tianshan suture zone, *TFF* Talas-Fergana fault. *Black rectangular* at south of Xiate marks the study area (Fig. 2)

west with the Nikolaev Line (Li and Li 1997; Li and Liu 1997). A short introduction of the evolution of the Yili, Central Tianshan, and Tarim plates as well as the NNF and STSZ is given below.

The Yili, Central Tianshan, and Tarim plates

The Yili plate is underlain by Mezo- to Neo-Proterozoic basement (schist, marble and quartzite, stromatolitic limestone and granitic gneiss), which is exposed as discrete blocks along the northern margin. It is overlain by Sinian-early Cambrian cover strata, which contain interlayers of limestone, siltstone, tillite and phosphoric silicate rocks (Coleman 1989; Allen et al. 1992; Che et al. 1994; Chen et al. 1999). Middle Cambrian—early Ordovician strata are lacking. Silurian neritic clastic rocks, carbonates and interbedded intermediate-acid volcanic rocks and Devonian–Carboniferous subaerial mafic-intermediate volcanites crop out on the northern and southern parts of the plate and are generally considered to have formed at the active continental margins of the Paleo-Junggar and the South Tianshan oceans, respectively (Coleman 1989; Windley et al. 1990; Gao et al. 1998, 2006; Qian et al. 2006; Zhu et al. 2006). The overlying Permian strata are made up of continental clastic rocks and post-collisional rifting volcanites (Zhao et al. 2003).

To the west the Yili plate adjoins the Issyk plate in the Kyrgyzstan North Tianshan, which is underlain by Proterozoic basement (Milanovsky 1996). Cambrian to lower Arenigian rocks are considered to be remnants of the Terskey ocean and consist of subduction-related volcanites, marginal sea, rift, and passive margin complexes in the Kyrgyzstan North Tianshan. They are unconformably overlain by middle Arenigian conglomerates and olistostromes and upper Arenigian–lower Caradocian arc-type volcanites or clastic rocks, which in turn are overlain disconformably by upper Ordovician red sandstones with siltstone and limestone interlayers. These rocks are covered unconformably by Devonian subaerial volcanites, Carboniferous redbeds, conglomerates and sandstones, as well as Permian volcanites (Bazhenov et al. 2003).

The Central Tianshan plate is underlain by middle to late Proterozoic basement, which is composed of gneisses, schists, migmatites and marbles and covered by Sinian carbonates and tillites (Che et al. 1994; Milanovsky 1996; Li and Li 1997; Li and Liu 1997). Cambrian–Ordovician rocks are made up of carbonates and flysch in Kyrgyzstan (Milanovsky 1996), but are absent in the Chinese segment. Arc-type granites and volcanics of Silurian-early Carboniferous age are extensively exposed in the Chinese Central Tianshan plate (Gao et al. 2006).

The Tarim plate is underlain by Archean and Proterozoic metamorphic basement (gneisses, schists, marbles, quartzites, and stromatolitic limestones), which is covered disconformably by Sinian shallow marine clastic rocks, carbonates, tillites and lower Cambrian black shales and phosphoric silicate rocks (Allen et al. 1992; Gao et al. 1998; Chen et al. 1999; Jiang et al. 2001). Cambrian–Devonian rocks are successive deposits on a stable marine platform, overlain unconformably or disconformably by Carboniferous marine/non-marine carbonates and clastics, as well as continental molasse and rift alkaline volcanics of Permian age (Allen et al. 1992; Carroll et al. 1995; Jiang et al. 2001).

The North Natali Fault (NNF) and South Tianshan Suture Zone (STSZ)

The NNF, also known as the Adengbulake–Lardun fault, is made up of polydeformed mylonites, gneisses and minor gabbroic and ultramafic rocks (Li and Li 1997; Li and Liu 1997). The fault continues for more than 450 km in China until it is truncated by the North Tianshan suture zone. Although it was formerly proposed to be the eastern extension of the Nikolaev Line, it has also been regarded as a secondary fault of the STSZ but not as an independent suture zone (Li and Li 1997; Li and Liu 1997). Consequently, the Chinese region between the North Tianshan and South Tianshan suture zones, denominated either as the Yili–Central Tianshan plate, the Central Tianshan plate or the Yili plate, has always been treated as a single plate (Allen et al. 1992; Carroll et al. 1995; Gao et al. 1998; Chen et al. 1999). In this paper however, the so-called Yili–Central Tianshan plate is suggested to comprise two distinct plates, the Yili and the Central Tianshan plates, which are separated by the NNF (Fig. 1). In the present study we provide evidence, that the NNF is an independent early Paleozoic suture zone.

The STSZ, also known as the Qinbulak–Qawabulak or South Nalati fault (Allen et al. 1992, Li and Li 1997), connects with the Atbashi–Inylchek fault in Kyrgyzstan (Solomovich and Trifonov 2002; He and Xu 2004). This suture zone marks the southern boundary of the Altaids. To the north of the STSZ a magmatic arc is superimposed on the Central Tianshan plate. To the south, ophiolites and high pressure–low temperature (HP-LT) metamorphic rocks occur in the South Tianshan fold belt. They were thrusted onto the passive continental margin sediments of the Tarim plate (Windley et al. 1990; Allen et al. 1992; Gao et al. 1998, 2006; Gao and Klemd 2003; Klemd et al. 2005). The arc rocks and ophiolites document the northward subduction of the STO (Windley et al. 1990; Allen et al. 1992; Gao et al. 1998, 2006).

The here investigated samples were collected at the south of the Xiate village in the southwestern Tianshan region of China (Fig. 2). Massive basaltic rocks were intruded by a dioritic pluton. Adjacent to the contacts, the basalts developed a hornfels texture as a result of contact metamorphism. Due to the absence of radiometric and stratigraphical data and the presence of late Paleozoic magmatic rocks in this region, the basalts and diorites were formerly designated as early Carboniferous volcanic and Hercynian plutonic rocks, respectively (BGXP 1981). Few geological studies were undertaken on these rocks. The basalts are covered by early Carboniferous limestone (BGXP 1981). The basalts, diorites, schists and early Carboniferous limestones are intruded by a late Paleozoic coarse K-feldspar megacrystic granite batholith (BGXP 1981). Precise formation age of the granite batholith is unclear. Similar K-feldspar granites from south Tekes yield single zircon U–Pb ages ranging between 280 and 266 Ma and are considered to be post-collisional (Gao et al. 2006).

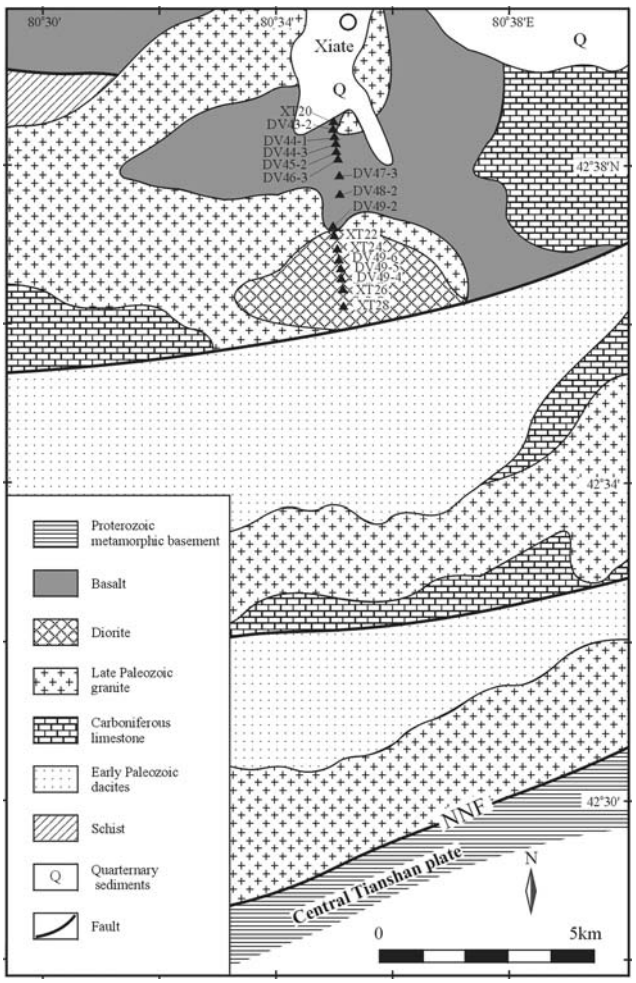

Fig. 2 Geological map of the Xiate area, southwestern Tianshan, China (modified after BGXP 1981). *NNF* North Nalati fault. *Black triangles* show sample localities

Fieldwork, sample description and analytical methods

Basalts (e.g., DV47-3, DV48-2) sampled at a distance of up to 1–2 km from the granitic intrusions still display-quenching textures and contain accessory plagioclase microphenocrysts. Those samples (e.g., XT20, DV43-2, DV44-3, DV46-3) collected near the K-feldspar megacrystic granite pluton underwent a greenschist facies metamorphic overprint and predominantly comprise albite, chlorite, epidote and actinolite, with occasionally preserved pseudomorphs of plagioclase and clinopyroxene phenocrysts. Basalts (e.g., DV49-2) collected near the dioritic pluton underwent hornblende–hornfels facies contact metamorphism. They display a mosaic texture and are made up of plagioclase, hornblende, minor biotite (<1%) and accessory iron oxides (up to ~5%) and titanite. Plagioclase and hornblende occur slightly orientated. The diorite consists of quartz, alkali feldspar, plagioclase, hornblende and minor biotite and has a well-preserved granular texture. Accessory minerals are apatite, titanite, iron oxide and zircon. The samples are generally unaltered, whereby the feldspars are slightly sericitized in places.

The sensitive high-resolution ion microprobe (SHRIMP) analyses were performed on the SHRIMP II instrument at Beijing SHRIMP Center in Chinese Academy of Geological Sciences (CAGS). Zircons were selected from crushed basalt (DV44-3) and diorite (DV49-5) samples by a combination of heavy liquid and magnetic separation techniques. Individual crystals were mounted in epoxy resin discs together with pieces of the Canberra standard TEMORA (417 Ma; Black et al. 2003). The discs were polished and zircons were half sectioned, followed by cleaning and gold coating. Cathodoluminescence (CL) images were taken by the Hitachi S-3000N Scanning Electron Microscope at CAGS for sample DV44-3 (Fig. 3) and by the CAMECA SX51 Electron Microscope at the Institute of Geology and Geophysics, Chinese Academy of Sciences (IGGCAS) for sample DV49-5 (Fig. 5), respectively. Spot sizes for the SHRIMP analyses averaged at about 30 μm and mass resolution at about 5,000 for measuring Pb/Pb and Pb/U isotopic ratios. The ^{238}U concentrations were normalized to the standard SL13 (^{238}U = 238 ppm; age: 572 Ma). The analyses of standard TEMORA and samples were alternated (1:3) for correcting Pb^+/U^+ discrimination. The data reported in Table 1 are corrected by assuming $^{206}Pb/^{238}U$–$^{208}Pb/^{232}Th$ age-concordance. The SQUID (Version 1.03d) and ISOPLOT (Version 3.00) programs of K.R. Ludwig were used to process the data.

After careful microscopic investigation 16 representative samples were selected for chemical analysis. They were crushed by a hardened jaw crusher, hand-picked, and then grinded in an agate mill into a powder with a grain size less than 200 mesh (~80 μm). Major oxides were

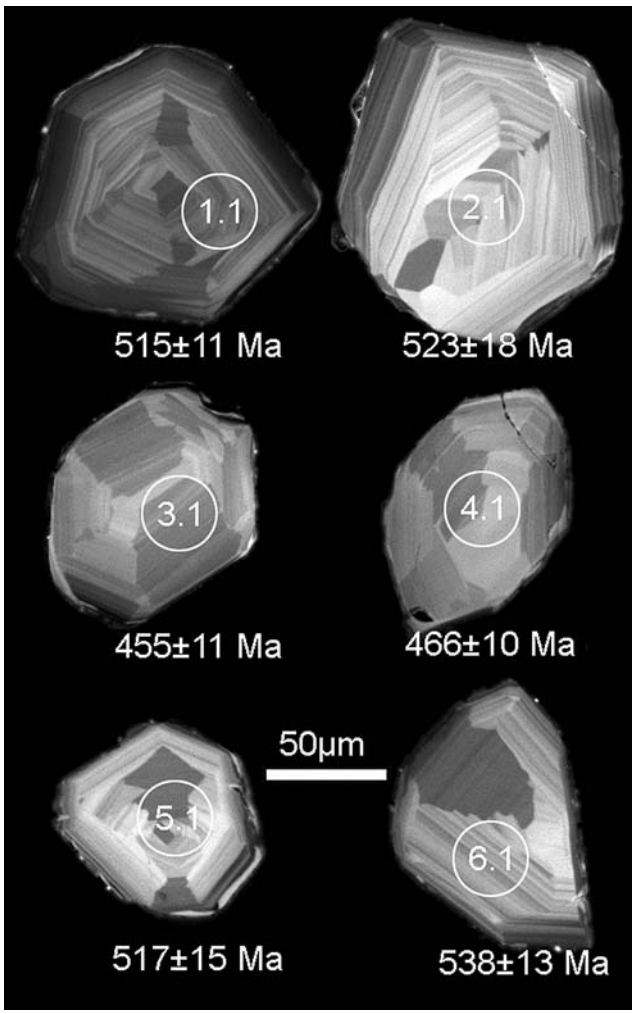

Fig. 3 Cathodoluminescence (*CL*) images of typical zircons from the Xiate basalt (DV44-3), southwestern Tianshan. *Circled spots* show position of SHRIMP analytical sites with their identification numbers. *Numbers* are $^{206}Pb/^{238}U$ ages listed in Table 1

determined by X-ray fluorescence spectrometry (XRF) on fused glass disks, using PHILLIPS PW1480 at Institute of Mineralogy of Universität Würzburg in Germany and Rigaku RIX2100 at Key Laboratory of Continental Dynamics in Northwest University in China. Uncertainties for most major oxides are <2%, for MnO and P_2O_5, <5%, and totals are within 100 ± 1%. Loss on ignition (LOI) was measured after heating to 1,000°C. Trace element concentrations were analyzed by inductively coupled plasma mass spectrometry (ICP-MS; Finnigan Element) at IGGCAS in Beijing. The detailed analytical procedure is the same as used by Qian et al. (2006). Relative standard deviations (RSD) are within ±10% for most trace elements but reach ±20% for V, Cr, Co, Ni, Th and U according to analysis of rock standards.

Sr and Nd isotope analyses were performed in the Laboratory of Radiogenic Isotope Geochemistry at IGGCAS by thermal ionization mass spectrometry (TIMS) using a Finnigan MAT 262 mass spectrometer. The detailed analytical process follows that of Qian et al. (2006). Nd and Sr isotope ratios were normalized to $^{146}Nd/^{144}Nd = 0.7219$ and $^{86}Sr/^{88}Sr = 0.1194$, respectively for correction of mass fractionation. The NBS987 Sr standard yielded $^{87}Sr/^{86}Sr = 0.710237 \pm 13$ (2σ), and the Ames Nd standard yielded $^{143}Nd/^{144}Nd = 0.512144 \pm 14$ (2σ). Total procedural Standard BCR-1 yielded $^{143}Nd/^{144}Nd$ value of 0.512633 ± 12 (2σ) and $^{87}Sr/^{86}Sr$ value of 0.705013 ± 11 (2σ).

Analytical results

Zircon U–Pb data

Zircon grains from sample DV44-3 of the Xiate basalt are euhedral, equant or fragments, which have clear thin oscillatory growth zoning as shown by the CL images (Fig. 3). 15 points analyzed on 14 separate zircon grains are listed in Table 1 and the results are shown on a concordia plot in Fig. 4a. With the exception of two discordant grains (spots 4.1 and 10.1) and one concordant grain (spot 3.1) giving a $^{206}Pb/^{238}U$ age of 455 ± 11 Ma, the remaining 12 analytical points show a tight, concordant group defining a weighted mean $^{206}Pb/^{238}U$ age of 516.3 ± 7.4 Ma (Fig. 4b). Grains 3.1 and 4.1 with the youngest $^{206}Pb/^{238}U$ ages have blurred oscillatory zoning, which probably indicates the disturbance of the U–Pb isotopic systems due to subsequent magmatism or metamorphism.

Zircon grains from sample DV49-5 of the Xiate dioritic pluton are euhedral and elongate-prismatic with angular terminations and an average length to width ratio of about 2.5. The CL images show oscillatory growth zoning typical of igneous rocks (Fig. 5). In total 19 measurements were made on 16 zircon grains. The results are presented in Table 1 and shown on concordia and weighted mean diagrams (Fig. 6). The grains are low in U (76–214 ppm) and Th (33–158 ppm), with $^{232}Th/^{238}U$ ratios varying between 0.37 and 0.99. The percentage of common Pb is generally low. Most of the analyses are concordant and tightly clustered (Fig. 6a). Apart from two discordant grains (7.1 and 10.1), the remaining 17 concordant grains yield a weighted mean $^{206}Pb/^{238}U$ age of 470 ± 12 Ma (Fig. 6b), which is interpreted as the crystallization age of the dioritic rocks.

Major and trace elements

Major and trace element data of the basalts and diorites are presented in Table 2. The basalts are characterized by low Al_2O_3 (12.72–14.05%) and P_2O_5 (0.14–0.22%), high total

Table 1 U–Th–Pb SHRIMP data for basalt (DV44–3) and diorite (DV49-5) samples, from Xiate in Tianshan (NW China)

Spot no.	$^{206}Pb_c$ (%)	U (ppm)	Th (ppm)	$^{232}Th/^{238}U$	$^{207}Pb^*/^{206}Pb^*$	$^{207}Pb^*/^{235}U$	$^{206}Pb^*/^{238}U$	$^{206}Pb/^{238}U$ age (Ma)
Sample DV44-3:								
1.1	2.14	80	37	0.47	0.0581 ± 8.3	0.666 ± 8.5	0.0832 ± 1.9	515 ± 11
2.1	4.72	41	16	0.42	0.0692 ± 10	0.806 ± 11	0.0845 ± 3.1	523 ± 18
3.1	2.06	91	59	0.67	0.0629 ± 5.8	0.634 ± 6.2	0.0731 ± 2.0	455 ± 11
4.1	1.61	82	46	0.58	0.0484 ± 4.3	0.501 ± 4.7	0.0750 ± 2.0	466 ± 10
5.1	5.00	41	20	0.52	0.0620 ± 19	0.720 ± 19	0.0835 ± 2.4	517 ± 15
6.1	3.01	56	28	0.52	0.0616 ± 5.2	0.739 ± 5.6	0.0870 ± 2.1	538 ± 13
7.1	1.52	87	45	0.54	0.0613 ± 3.4	0.717 ± 3.9	0.0848 ± 1.9	525 ± 11
8.1	2.52	58	23	0.42	0.0588 ± 6.7	0.671 ± 7.0	0.0829 ± 2.2	513 ± 12
8.2	4.32	41	17	0.43	0.0640 ± 16	0.690 ± 16	0.0791 ± 2.3	491 ± 13
10.1	2.53	77	35	0.47	0.0667 ± 3.5	0.783 ± 4.0	0.0852 ± 2.0	527 ± 11
11.1	4.54	38	15	0.42	0.0557 ± 8.9	0.659 ± 9.2	0.0857 ± 2.4	530 ± 15
12.1	3.45	55	21	0.40	0.0522 ± 5.3	0.593 ± 5.7	0.0823 ± 2.1	510 ± 12
13.1	5.81	44	19	0.44	0.0659 ± 7.4	0.735 ± 7.7	0.0808 ± 2.4	501 ± 14
14.1	4.46	46	23	0.51	0.0598 ± 15	0.670 ± 15	0.0816 ± 2.4	506 ± 15
15.1	4.42	42	25	0.61	0.0567 ± 13	0.667 ± 13	0.0853 ± 2.3	528 ± 14
Sample DV49-5:								
1.1	5.64	87	41	0.49	0.0539 ± 11	0.528 ± 11	0.0709 ± 4.1	442 ± 20
2.1	5.03	80	39	0.50	0.0636 ± 13	0.659 ± 14	0.0751 ± 3.6	467 ± 19
2.2	3.38	167	60	0.37	0.0485 ± 9.1	0.529 ± 9.9	0.0792 ± 3.8	491 ± 20
3.1	3.84	114	44	0.40	0.0561 ± 9.4	0.654 ± 10	0.0846 ± 3.6	524 ± 20
4.1	3.42	133	99	0.77	0.0538 ± 9.5	0.552 ± 10	0.0744 ± 3.4	463 ± 18
5.1	5.10	87	37	0.45	0.0495 ± 7.9	0.510 ± 8.7	0.0748 ± 3.6	465 ± 19
6.1	4.66	96	56	0.61	0.0535 ± 17	0.566 ± 17	0.0769 ± 3.5	477 ± 19
7.1	2.48	90	46	0.53	0.0738 ± 7.3	0.691 ± 8.2	0.0679 ± 3.7	423 ± 18
8.1	3.60	134	71	0.55	0.0523 ± 5.7	0.532 ± 6.7	0.0738 ± 3.4	459 ± 17
9.1	6.79	80	41	0.53	0.0530 ± 13	0.542 ± 14	0.0742 ± 3.6	461 ± 20
10.1	1.44	138	104	0.77	0.0910 ± 14	1.010 ± 15	0.0807 ± 3.5	501 ± 26
10.2	4.19	76	33	0.46	0.0632 ± 15	0.615 ± 16	0.0706 ± 4.2	440 ± 20
11.1	3.63	103	47	0.47	0.0629 ± 6.9	0.704 ± 7.7	0.0811 ± 3.5	503 ± 19
12.1	13.11	152	145	0.99	0.0450 ± 82	0.450 ± 82	0.0712 ± 3.5	443 ± 30
13.1	2.02	214	158	0.76	0.0548 ± 6.8	0.548 ± 7.5	0.0726 ± 3.3	452 ± 17
13.2	2.97	112	77	0.71	0.0575 ± 9.3	0.629 ± 9.9	0.0793 ± 3.5	492 ± 19
14.1	1.55	109	80	0.76	0.0703 ± 7.9	0.732 ± 8.6	0.0756 ± 3.5	470 ± 19
15.1	5.37	102	71	0.73	0.0482 ± 11	0.469 ± 13	0.0705 ± 5.3	439 ± 27
16.1	4.98	105	74	0.73	0.0607 ± 7.0	0.668 ± 9.3	0.0798 ± 6.1	495 ± 35

Errors are 1σ. Pb_c and Pb* indicate common and radiogenic Pb, respectively. Common Pb corrected by assuming $^{206}Pb/^{238}U$–$^{208}Pb/^{232}Th$ age-concordance

Fe (12.89–16.03% as Fe_2O_3) and moderate TiO_2 (1.44–2.24%) and MgO (5.88–7.83%) contents. As described in the previous section, the basalts experienced varying degrees of metamorphism, which may have caused changes regarding the major element concentrations. However TiO_2 and P_2O_5 are generally considered to be immobile (Rollinson 1993). Chemical changes during contact metamorphism are substantiated by the observation that K_2O contents are moderately elevated in the greenschist facies samples (0.29–0.41%) and highly enriched in the hornblende–hornfels facies samples (~0.80%). However, most other major elements are interpreted to have maintained their primary magmatic values, as is evidenced by similar values of all samples as well as by the systematic covariations between the major oxides and their ratios (Fig. 7). The basalts are sub-alkaline and tholeiitic. Most samples are olivine normative (1.2–10.2 wt% assuming molar Fe^{2+}/total Fe = 0.85), except one sample (XT20), which contains minor normative quartz (1.61%). In terms of their major element composition, the rocks are similar to mid-ocean ridge basalts (MORB) (le Roex et al. 1982; Altherr et al. 1988; Reynolds et al. 1992; Debaille et al.

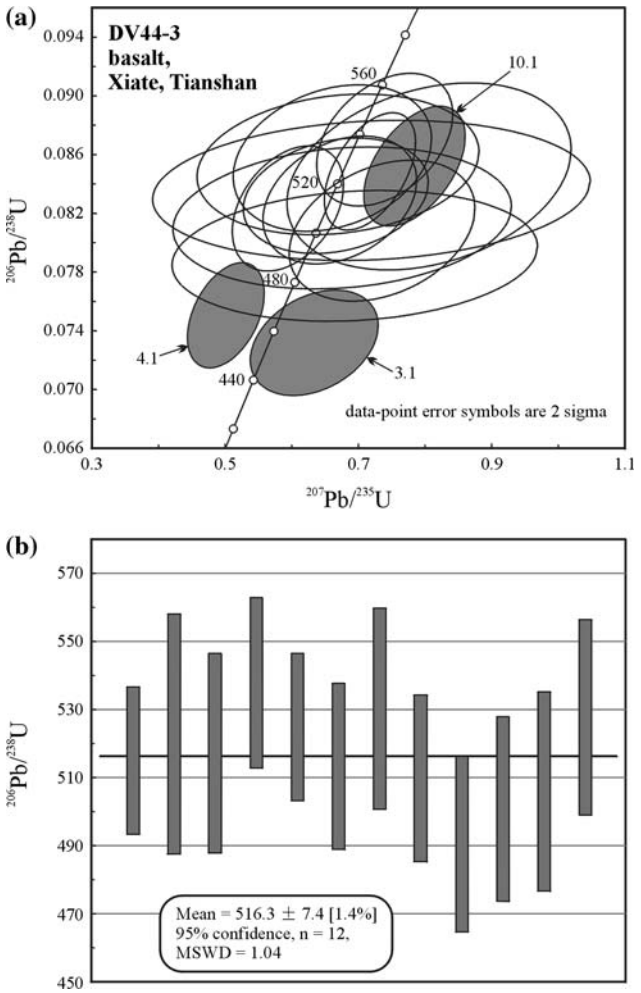

Fig. 4 $^{207}Pb/^{235}U$–$^{206}Pb/^{238}U$ concordia diagram (**a**) and weighted average diagram (**b**) of the Xiate basalts (sample DV44-3) from southwestern Tianshan

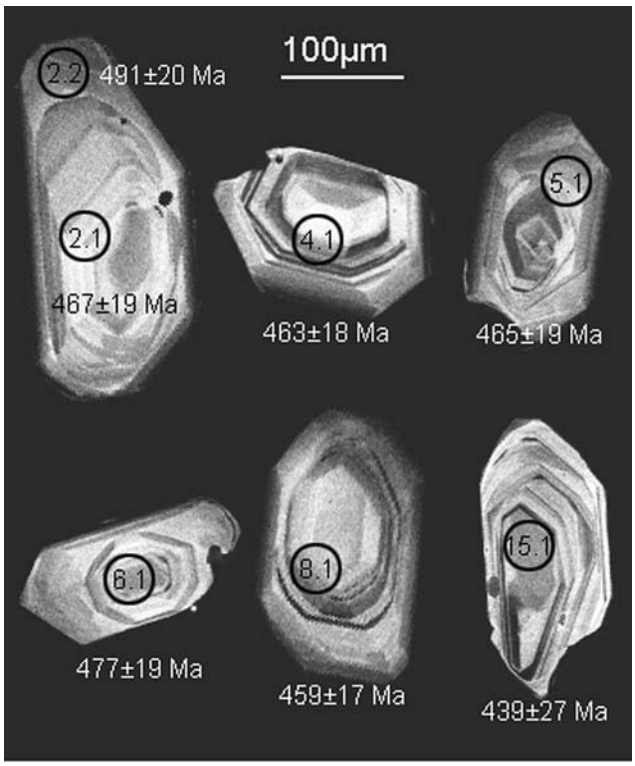

Fig. 5 Cathodoluminescence (*CL*) images of typical zircons from the Xiate diorites (DV49-5), southwestern Tianshan. *Circled spots* show position of SHRIMP analytical sites with their identification numbers. *Numbers* are $^{206}Pb/^{238}U$ ages listed in Table 1

2006). Four of the basalts have $TiO_2 > 2\%$, $FeO^t > 12\%$ and $FeO^t/MgO > 1.75$, and can be classified as FeTi-basalt or ferrobasalt (le Roex et al. 1982; Sinton et al. 1983; Harper 2003). The systematic covariations between major oxides also suggest a cogenetic origin by fractional crystallization, which lead to moderate to low Mg# values (47–57). Clinopyroxene fractionation is indicated by the positive correlation of the CaO/Al_2O_3 ratios and the CaO contents (Fig. 7d). Of these rocks, the ferrobasalts are the most highly evolved as is indicated by their Mg# values, which range between 47 and 50.

Chondrite-normalized REE patterns of the basaltic rocks are flat (Fig. 8b) and are similar to those of typical T-MORB (Sun et al. 1979). $(La/Sm)_N$ ratios (0.71–1.06) are greater than that of typical N-MORB (0.4–0.7) but lie within the range of T-MORB (Sun et al. 1979; Reynolds et al. 1992). Plagioclase fractionation is indicated by variable Eu negative anomalies ($Eu/Eu^* = 0.86–0.99$). In an N-MORB normalized multi-element spidergram (Fig. 8a), moderate incompatible elements (Nd to Lu) are evenly distributed, while Nb, Ta, La and Ce are slightly enriched. The Ti/Zr (78–124), Zr/Y (2.7–3.6) and TiO_2/P_2O_5 (9.5–11.4, one sample 15.7) ratios are consequently close to those of MORB (100 ± 10, 2.5 and 10, respectively) and chondrite (Sun et al. 1979; Sun and McDonough 1989). Since Nb, Zr and Y show a similar compatibility as the light, middle and heavy REE respectively (Sun and McDonough 1989), Zr/Nb and Y/Nb ratios may reflect the patterns of the REE. For the basaltic rocks, Y/Nb (6.2–7.0) ratios are chondritic (~6.4) and Zr/Nb (16.8–23.0) ratios are between that of chondrite (~16) and N-MORB (~37, Sun et al. 1979), both showing T-MORB affinity in accordance with the REE patterns. The Nb/La (0.74–1.27) and Th/Ta (0.52–1.67) ratios are confined within the ranges of that of chondrite, primitive mantle and MORB (Sun and McDonough 1989), while continental crust and arc basalts are normally characterized by remarkable Nb and Ta negative anomalies and high Th/Ta ratios (Rudnick 1995; Condie 1997). Enrichment in mobile elements such as Rb, Ba and K could be caused by alteration and/or metamorphism, which is supported by positive correlations between Rb and K, and Ba and Sr. Low Cr (75.0–190.7 ppm) and Ni (38.6–73.5 ppm) contents and their positive covariation may result from olivine and pyroxene fractionation. The

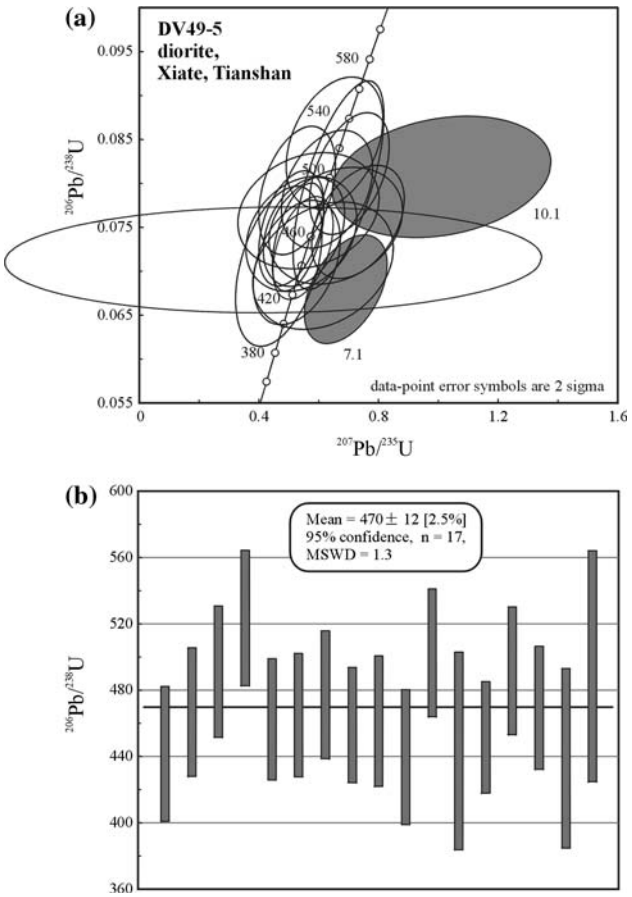

Fig. 6 $^{207}Pb/^{235}U$–$^{206}Pb/^{238}U$ concordia diagram (**a**) and weighted average diagram (**b**) of the Xiate diorites (sample DV49-5) from southwestern Tianshan

ferrobasalts contain the lowest Cr and Ni contents, consequently, in accordance with the Mg# values, they are interpreted to be the most highly evolved rocks investigated here. It is notable that the Zr/Hf (33.4–35.4) and Nb/Ta (14.0–17.8) ratios resemble those of MORB (Sun and McDonough 1989), thereby supporting the assumption, that the zircon grains used for SHRIMP analyses crystallized during the basaltic magma evolution.

The diorite samples are meta-aluminous [molar $Al_2O_3/(Na_2O + K_2O + CaO) = 0.9–1.0$] and sodic ($K_2O/Na_2O$ = 0.2–0.9), with silica contents ranging from about 60–69 wt%. In the Streckeisen QAP diagram (Fig. 9a), they define a crude calc-alkaline trend (e.g., Lameyre and Bowden 1982) and are classified as quartz monzodiorite (XT24, DV49-4, DV49-5 and DV49-6), granodiorite (XT22 and XT26) and quartz diorite (XT28). They furthermore show a tonalitic and granodioritic character in the normative Ab–An–Or diagram (Fig. 9b). Despite some variations in the classifications, the samples show similar major and trace elemental characteristics such as high Al_2O_3 (15.89–20.58%), Sr (531–712 ppm) and Ba (433–1,421 ppm) contents and low TiO_2 (0.23–0.50%), P_2O_5 (0.10–0.19%), Y (11.0–17.6 ppm), HREE (Yb = 1.18–2.09 ppm), Sc (3.4–9.5 ppm) contents. Furthermore, Sr/Y (39.5–58.7), La/Yb (9.1–16.8) ratios are relatively high, while Ga/Al ratios (10,000 Ga/Al = 1.2–2.0) are comparatively low. Additionally, the samples are characterized by a strong Nb, Ta, P and Ti depletion and Sr enrichment in the primitive mantle-normalized spidergram (Fig. 10a), as well as fractionated REE patterns (Fig. 10b) with positive or negligible Eu negative anomalies (Eu/Eu* = 0.94–1.45). These chemical characteristics resemble those of Cenozoic adakitic rocks (Figs. 10, 11). Adakitic rocks have geochemical signatures (e.g., $Al_2O_3 \geq 15\%$, Sr > 400 ppm, Y ≤ 18 ppm, Yb ≤ 1.9 ppm, Sr/Y > 40 and La/Yb > 10), which are similar to those of high-Al TTG (tonalite–trondhjemite–granodiorite) (Defant and Drummond 1990, 1993; Martin et al. 2005). Numerous experimental studies have shown that adakitic rocks can be formed by high-pressure (≥ca.10 kbar) partial melting (usually dehydration melting) of garnet amphibolite, eclogite or even granulite with residual assemblages composed of garnet, clinopyroxene and/or amphibole (Rapp et al. 1991; Sen and Dunn 1994; Wolf and Wyllie 1994; Rapp and Watson 1995; Foley et al. 2002). The consistent concave heavy rare earth elements (HREE) pattern (Fig. 10), the chondritic Y/Yb (8.5–10.1) ratios and the relatively high Zr/Sm (30.7–45.1) ratios of the dioritic rocks are compatible with an amphibole-dominated residue (Qian 2001; Foley et al. 2002), whereas garnet may also have been stable as is indicated by the superchondritic Gd_N/Yb_N (1.2–1.7) ratios (Martin et al. 2005). The high Sr values and lack of negative Eu anomalies require little plagioclase in the residue. The chemical composition of these rocks is similar to that of the so-called high-SiO_2 adakites of Martin et al. (2005), with regards to their high SiO_2 (>60 wt. %), low MgO (1.97–2.13 wt.%), Cr (<22 ppm), Ni (≤80 ppm), Mg# (37–47) and K/Rb (292–489) values.

Sr–Nd isotopes

Rb, Sr, Sm and Nd concentrations and Sr and Nd whole-rock isotopic compositions of selected basalt samples are listed in Table 3, together with initial $^{87}Sr/^{86}Sr$ and $^{143}Nd/^{144}Nd$ ratios and εNd(t) values, which were calculated for an age of 516 Ma. The εNd(t) values (+3.37 to +4.95) are lower than that of Bay of Islands ophiolite from the Appalachians (501–508 Ma, Jacobsen and Wasserburg 1979) and Chamrousse ophiolite from the Western Alps (497 Ma, Pin and Carme 1987). They are further lower than the 500 Ma depleted mantle value (ca. +7.1), which was calculated using the mantle evolution equation of DePaolo (1981). However, they are similar to some of the E-MORBs from the Mid-Atlantic Ridge

Table 2 Major (wt.%) and trace (ppm) element data of basalts and diorites from Xiate village, NW China

Rock type	Basalts							
Sample	DV43-2	DV44-1	DV44-3	DV45-2	DV46-3	DV47-3	DV48-2	DV49-2
SiO_2	50.22	49.13	48.65	49.38	49.94	49.15	50.03	48.89
TiO_2	1.76	2.35	2.12	1.71	2.24	1.62	1.44	1.59
Al_2O_3	13.42	13.35	12.97	13.04	13.35	14.05	13.91	13.22
Fe_2O_3	13.34	14.66	16.03	14.54	13.86	13.62	12.89	13.96
MnO	0.18	0.22	0.15	0.15	0.17	0.23	0.19	0.28
MgO	6.39	6.16	6.09	6.18	5.88	7.03	6.96	7.83
CaO	9.56	8.61	8.87	9.43	9.37	10	10.65	9.25
Na_2O	3.28	3.46	3.31	3.62	3.58	3.06	2.77	2.80
K_2O	0.40	0.43	0.29	0.37	0.41	0.22	0.20	0.80
P_2O_5	0.17	0.15	0.20	0.15	0.21	0.16	0.14	0.14
LOI	1.05	1.35	0.98	0.84	0.73	0.76	0.81	1.24
Total	99.77	99.87	99.66	99.41	99.74	99.90	99.99	100.00
Mg#	52	50	46	50	49	53	55	0.55
Li	8.12		4.88		4.94		7.55	18.6
Be	0.78		0.74		0.90		0.84	0.83
Sc	48.8		51.0		51.5		50.0	42.7
V	406		444		460		363	388
Cr	167		110		85.7		191	109
Co	52.1		39.0		42.2		45.2	49.0
Ni	73.5		66.5		55.9		71.4	68.5
Zn	87.9		74.3		81.1		102	119
Ga	18.3		18.2		20.7		16.7	16.5
Rb	9.80		6.50		13.2		5.79	26.2
Sr	157		157		166		154	176
Y	42.9		37.7		45.7		31.9	37.5
Zr	135		103		164		95.9	112
Nb	6.14		6.11		7.10		5.12	5.46
Cs	0.680		0.814		1.57		0.695	1.20
Ba	80.9		66.9		108		69.7	231
La	8.30		4.81		5.74		6.08	7.13
Ce	19.5		13.0		16.3		15.0	17.8
Pr	3.23		2.23		2.79		2.38	2.87
Nd	16.1		12.1		15.4		12.2	14.1
Sm	5.05		4.16		5.23		3.81	4.42
Eu	1.79		1.53		1.74		1.21	1.58
Gd	6.48		5.40		6.50		4.88	5.67
Tb	1.16		1.06		1.28		0.939	1.04
Dy	7.70		7.21		8.78		6.31	7.08
Ho	1.66		1.59		1.93		1.35	1.54
Er	4.71		4.43		5.47		3.78	4.40
Tm	0.709		0.667		0.812		0.564	0.671
Yb	4.54		4.23		5.16		3.61	4.38
Lu	0.687		0.641		0.790		0.555	0.677
Hf	4.02		3.05		4.70		2.87	3.32
Ta	0.437		0.364		0.450		0.327	0.306
Tl	0.093		0.081		0.137		0.067	0.161
Pb	3.27		2.33		2.88		2.24	4.82

Table 2 continued

Rock type	Basalts							
Sample	DV43-2	DV44-1	DV44-3	DV45-2	DV46-3	DV47-3	DV48-2	DV49-2
Th	0.730		0.189		0.674		0.479	0.401
U	0.244		0.108		0.248		0.181	0.257
Rock type	Basalts	Diorites						
Sample	XT20*	XT22*	XT24*	XT26*	XT28*	DV49-4	DV49-5	DV49-6
SiO_2	49.68	61.98	62.54	68.93	60.90	62.3	61.45	59.92
TiO_2	2.08	0.39	0.39	0.23	0.31	0.43	0.46	0.50
Al_2O_3	12.72	16.35	16.90	15.89	20.58	17.15	17.07	17.71
Fe_2O_3	14.93	5.60	5.03	2.82	3.93	5.45	5.61	6.07
MnO	0.19	0.08	0.11	0.06	0.06	0.1	0.13	0.15
MgO	5.91	2.00	1.97	1.04	1.06	1.95	2.08	2.13
CaO	9.72	5.71	5.45	3.34	4.90	5.59	5.49	6.72
Na_2O	2.73	3.20	3.81	3.90	6.30	3.55	3.15	3.87
K_2O	0.36	2.22	2.23	2.64	1.25	2.2	2.99	1.45
P_2O_5	0.22	0.19	0.19	0.10	0.12	0.17	0.17	0.19
LOI	1.09	1.92	0.90	0.69	0.55	0.96	0.97	0.73
Total	99.63	99.64	99.52	99.64	99.96	99.85	99.57	99.44
Mg#	47	44	47	45	37	44	45	44
Li	5.54	14.6	9.06	8.21	3.00	9.64	11.7	7.27
Be	0.80	1.14	1.12	1.40	2.14	1.61	1.21	1.44
Sc	47.6	7.11	9.53	3.75	3.41	7.32	7.12	9.49
V	436	107	94.7	36.6	43.1	102	112	124
Cr	75.0	4.83	2.92	0.687	7.7	10.6	21.9	18.9
Co	42.2	7.36	10.4	5.11	4.78	12.1	13.5	14.0
Ni	38.6	2.44	8.32	–	0.909	–	14.4	80.1
Zn	83.1	38.6	40.7	45.6	34.4	39.3	57.7	67.6
Ga	17.9	17.7	17.4	16.7	22.3	12.5	11.1	12.6
Rb	9.85	63.1	57.3	60.5	21.2	40.8	60.8	32.7
Sr	118	597	635	579	709	531	648	712
Y	43.2	12.4	13.6	12.2	16.9	13.4	11.0	17.6
Zr	140	111	117	108	161	125	98.6	121
Nb	6.35	6.45	6.66	6.17	4.71	6.62	4.99	8.39
Cs	0.315	2.15	1.69	2.46	0.680	1.08	1.84	1.38
Ba	38.2	703	901	1019	593	433	1421	450
La	7.63	17.1	13.6	15.7	19.6	19.6	19.8	28.4
Ce	20.4	29.9	29.4	29.5	34.4	34.9	31.9	51.3
Pr	3.11	3.52	3.65	3.38	4.22	3.90	3.59	5.86
Nd	15.4	13.2	14.0	12.7	16.3	15.5	13.9	24.5
Sm	4.93	2.56	2.70	2.60	3.63	2.76	2.43	3.95
Eu	1.72	0.772	0.819	0.706	1.37	0.946	1.17	1.63
Gd	6.43	2.24	2.22	2.02	3.08	2.63	2.49	3.66
Tb	1.23	0.359	0.369	0.341	0.529	0.424	0.354	0.592
Dy	8.05	2.02	2.07	1.93	3.00	2.56	2.17	3.74
Ho	1.74	0.414	0.445	0.415	0.617	0.452	0.392	0.612
Er	4.91	1.23	1.29	1.15	1.70	1.21	1.05	1.63
Tm	0.729	0.209	0.219	0.187	0.260	0.250	0.202	0.336
Yb	4.70	1.47	1.50	1.30	1.68	1.43	1.18	2.09

Table 2 continued

Rock type	Basalts	Diorites						
Sample	XT20*	XT22*	XT24*	XT26*	XT28*	DV49-4	DV49-5	DV49-6
Lu	0.742	0.232	0.239	0.204	0.255	0.270	0.210	0.350
Hf	3.96	2.91	3.01	2.90	4.04	3.54	2.95	3.70
Ta	0.403	0.477	0.463	0.386	0.250	0.504	0.344	0.713
Tl	0.085	0.282	0.220	0.280	0.119	–	–	–
Pb	1.45	9.30	9.49	16.6	11.3	6.42	8.55	9.06
Th	0.530	4.20	3.01	3.63	3.59	5.68	4.01	6.67
U	0.151	1.92	1.21	0.921	0.670	1.61	0.691	1.24

Mg# = 100Mg/(Mg + Fe^{2+}), assuming Fe^{2+} = 0.85 total Fe

*Major elements analyzed in Northwest University, China

(Debaille et al. 2006, and references therein). All samples have $(^{87}Sr/^{86}Sr)_i$ values (0.70428–0.70545) higher than that of present-day MORB (Sun et al. 1979; Ito et al. 1987) and plot to the right of the Mantle array in a $(^{87}Sr/^{86}Sr)_i$ versus εNd(t) diagram (Fig. 12). The elevation in $(^{87}Sr/^{86}Sr)_i$ ratios may be caused by seawater alteration which however only has a limited effect on the $^{143}Nd/^{144}Nd$ ratios (Jacobsen and Wasserburg 1979).

$(^{87}Sr/^{86}Sr)_i$ and εNd(t) values of the diorites were calculated using an age of 470 Ma. The diorites have moderately high $(^{87}Sr/^{86}Sr)_i$ values, ranging from 0.70526 to 0.70623. εNd(t) values (−4.46 to −1.32) are lower than that of the basalts (Table 3, Fig. 12a). Nd depleted mantle model ages (1.30–1.44 Ga) point to a magma source with an average middle-Proterozoic crustal-residence time, when supposing that the samples possess Nd isotopic

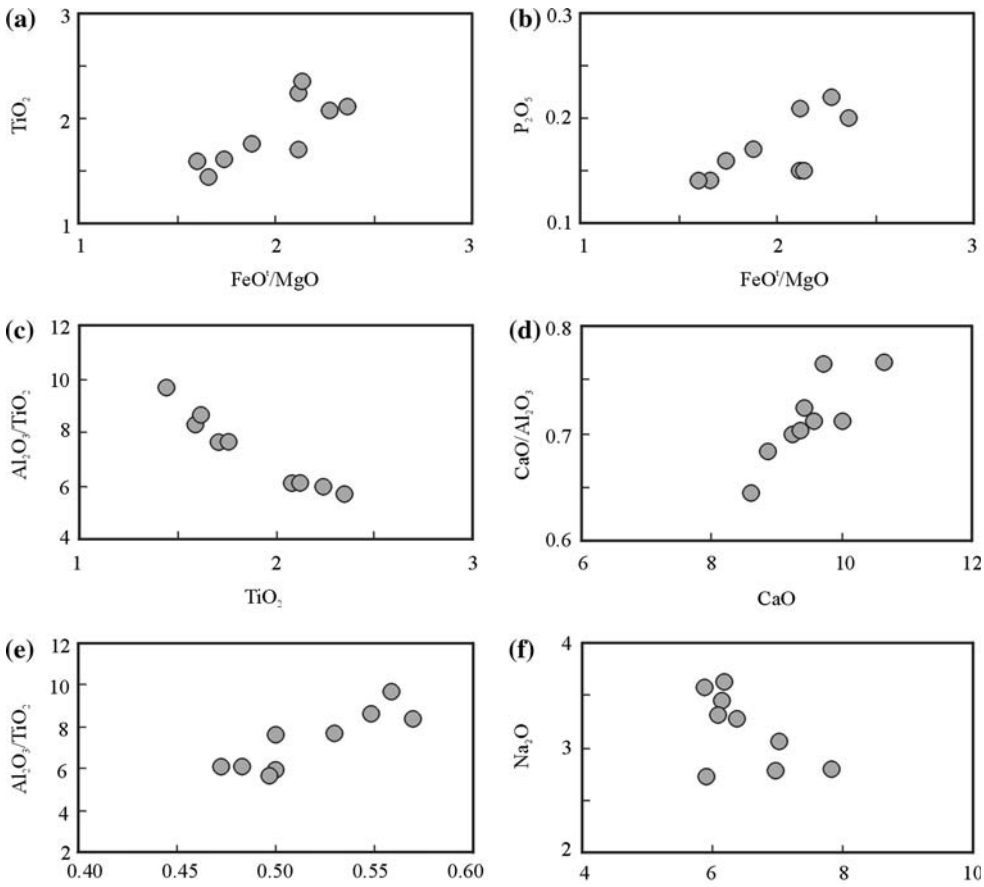

Fig. 7 Variation diagrams of TiO_2 versus FeO^t/MgO (**a**), P_2O_5 versus FeO^t/MgO (**b**), Al_2O_3/TiO_2 versus TiO_2 (**c**), CaO/Al_2O_3 versus CaO (**d**), Al_2O_3/TiO_2 versus Mg# (**e**), and Na_2O versus MgO (**f**) for samples from the Xiate basalts, southwestern Tianshan

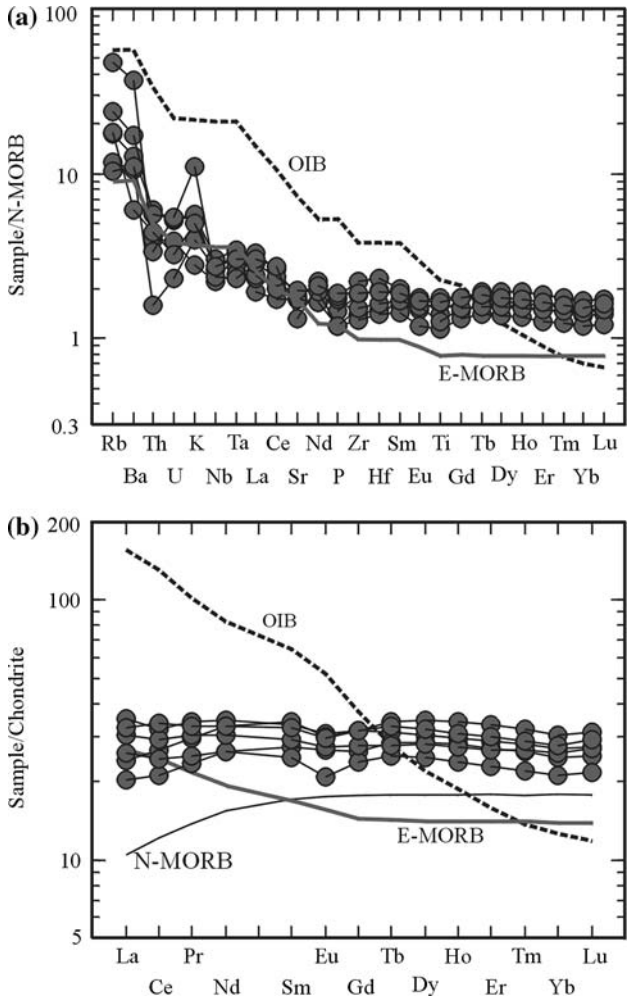

Fig. 8 **a** N-MORB normalized multi-element spidergram and **b** chondrite normalized REE distribution diagram for samples from the Xiate basalts, southwestern Tianshan. Data of N-MORB, E-MORB, OIB and chondrite from Sun and McDonough (1989)

compositions identical to their sources. The Sr and Nd isotopic characteristics and the T_{DM} values do not favor subducted oceanic crust as possible sources for the diorite, but instead partial melting of lower continental crust is more reasonable assumption (Fig. 12a). Crustal assimilation may have played a role during the magma emplacement as indicated by the negative correlation between εNd(t) and SiO_2 values (Fig. 12b).

Discussion on tectonic settings of basalts and diorites

Basalts

In various discrimination diagrams (Fig. 13) of relatively immobile incompatible elements such as Th, Nb, Ta, Zr, Hf, Y and REE (Pearce and Norry 1979; Condie 1997; John et al. 2003), the basalts consistently plot in the MORB field. This substantiates the geochemical data discussed before. We therefore conclude that a mid-ocean ridge is the most probable formational setting for the basalts.

T-MORB in the Red Sea, which is transitional between a continental and an oceanic rift, represents lower degrees of partial melting in the mantle asthenosphere compared to N-MORB. Furthermore, T-MORB originates at the axial trough as embryonic oceanic crust flanking the central segment N-MORB on both the north and south side (Altherr et al. 1988; Petrini et al. 1988). Yet present-day T-MORB is also produced at transitional ridge segments of the Mid-Atlantic Ridge and the East Pacific Rise (Sun et al. 1979; Reynolds et al. 1992). Consequently, it is difficult to infer merely by their geochemical characteristics, whether the basalts were formed at spreading centers of a fully evolved ocean or an embryonic ocean such as the Red Sea.

Ferrobasalts have been reported from mid-ocean ridges (le Roex et al. 1982; Sinton et al. 1983) and some ophiolites (e.g., Harper 2003). At modern spreading ridges, ferrobasalts are predominantly associated with advancing tips of propagating rifts and are highly differentiated products under special conditions of closed-system

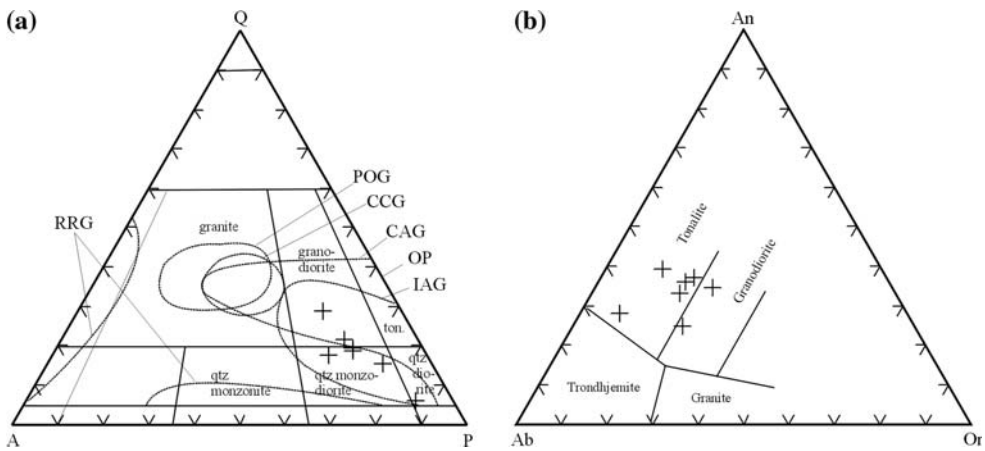

Fig. 9 **a** Quartz–alkali feldspar–plagioclase (*QAP*) diagram and **b** anorthite–albite–orthoclase (*An–Ab–Or*) diagram for samples from the Xiate dioritic pluton, southwestern Tianshan. Areas of rift-related granitoids (*RRG*), post-orogenic granitoids (*POG*), continental collision granitoids (*CCG*), continental arc granitoids (*CAG*), island arc granitoids (*IAG*) and oceanic plagiogranites (*OP*) in (**a**) are after Maniar and Piccoli (1989)

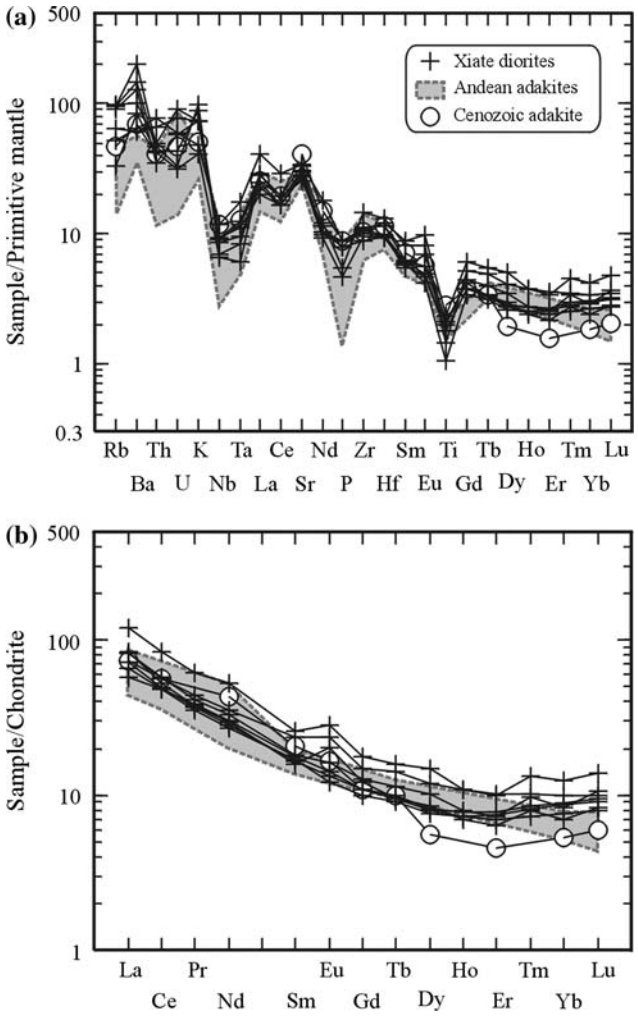

Fig. 10 **a** N-MORB normalized multi-element spidergram and **b** chondrite normalized REE distribution diagram for samples from the Xiate dioritic pluton, southwestern Tianshan. Normalizing data from Sun and McDonough (1989). Data of Andean adakites and Cenozoic adakite are after Stern and Kilian (1996) and Drummond et al. (1996), respectively

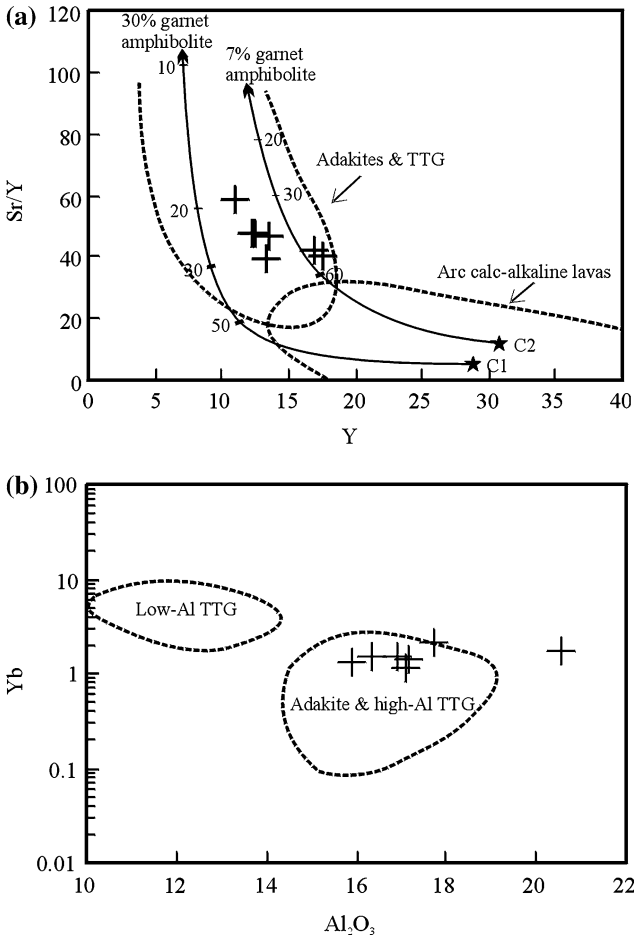

Fig. 11 **a** Sr/Y versus Y diagram (Petford and Atherton 1996) and **b** Yb versus Al_2O_3 diagram (Sheppard et al. 2001) for samples from the Xiate diorites, southwestern Tianshan

fractionation, low oxidation state and low magma supply rate (le Roex et al. 1982; Sinton et al. 1983; Harper 2003).

Diorites

In the Rb versus Y + Nb and Nb versus Y diagrams (Fig. 14) and the QAP diagram (Fig. 9a), the diorite samples plot tightly in the field of volcanic arc granite. In addition, the adakitic characteristics of the diorites may be used for deciphering the petrogenesis of these rocks. Initially adakitic rocks were denominated to describe intermediate-felsic rocks derived from partial melting of subducted oceanic crust under high-pressure conditions (Defant and Drummond 1990; Kay et al. 1993). Later studies, however, have shown that rocks with comparable major and trace elemental characteristics could be formed by partial melting (occasionally coincident with delamination) of thickened lower crust in arc settings (Muir et al. 1995; Petford and Atherton 1996; Wareham et al. 1997). Adakitic rocks are also reported to have formed via partial melting of thickened lower continental crust in non-arc settings (Waight et al. 1998; Xu et al. 2002; Gao et al. 2004; Topuz et al. 2005; Wang et al. 2005). The Sr and Nd isotopic composition of the Xiate diorites indicates lower thickened continental crust of either an arc or non-arc environment to be a possible magma source, yet subducted oceanic crust an unlikely source (Fig. 12).

Early Paleozoic tectonic evolution of the Chinese South Tianshan orogen

NNF, an early Paleozoic suture zone

Tectonic analyses have shown that the NNF connects to the west with the Nikolaev Line (Li and Li 1997; Li and Liu

Table 3 Rb–Sr and Sm–Nd isotopic data of the Xiate basalts and dioritic rocks, western Tianshan Mountains

Sample	Rock type	Rb (ppm)	Sr (ppm)	$^{87}Rb/^{86}Sr$	$^{87}Sr/^{86}Sr$	2σ	$(^{87}Sr/^{86}Sr)_i$	Sm (ppm)	Nd (ppm)	$^{147}Sm/^{144}Nd$	$^{143}Nd/^{144}Nd$	2σ	$(^{143}Nd/^{144}Nd)_i^a$	$\varepsilon Nd(t)^{a,b}$	$T_{DM}(Ga)^b$	$f_{Sm/Nd}$
DV44-3	Basalt	6.57	154	0.1218	0.706348	14	0.70545	3.78	10.8	0.211055	0.512908	12	0.512195	4.33	–	0.07
DV46-3	Basalt	12.69	155	0.2366	0.706677	20	0.70494	4.61	12.7	0.219903	0.512904	10	0.512161	3.66	–	0.12
DV48-2	Basalt	5.40	141	0.1101	0.705584	13	0.70477	3.22	10.1	0.194027	0.512860	13	0.512204	4.51	–	−0.01
DV49-2	Basalt	24.82	168	0.4282	0.708015	18	0.70487	4.08	12.2	0.202426	0.512830	7	0.512146	3.37	–	0.03
XT20	Basalt	7.86	124	0.1826	0.705623	11	0.70428	4.76	15.5	0.185830	0.512855	14	0.512227	4.95	–	−0.06
XT24	Qtz monzodiorite	56.06	650	0.2476	0.706959	14	0.70530	2.57	13.4	0.116444	0.512194	13	0.511835	−3.85	1.38	−0.41
XT26	Granodiorite	60.23	608	0.2843	0.707246	13	0.70534	2.27	11.7	0.117729	0.512167	11	0.511804	−4.46	1.44	−0.40
XT28	Qtz diorite	20.13	746	0.0773	0.706744	14	0.70623	3.41	15.9	0.129793	0.512365	9	0.511965	−1.32	1.30	−0.34
DV49-4	Qtz monzodiorite	62.74	597	0.3041	0.707330	18	0.70529	2.64	13.3	0.119760	0.512221	10	0.511852	−3.52	1.38	−0.39
DV49-5	Qtz monzodiorite	71.03	683	0.3010	0.707277	20	0.70526	2.10	10.8	0.117606	0.512212	8	0.511850	−3.56	1.37	−0.40

[a] Age corrected to 516 Ma for basalts, and 470 Ma for diorites, respectively

[b] $^{143}Nd/^{144}Nd$ and $^{147}Sm/^{144}Nd$ ratios are 0.513150, 0.222 and 0.512638, 0.1967 for modern depleted mantle and chondrite, respectively

1997). According to Lomize et al. (1997), ophiolites of Cambrian–early Ordovician age, representing remnants of the Terskey oceanic crust, are distributed within an area of about 500 km in length and tens of kilometers in width in the Kyrgyzstan Northern Tianshan region, to the north of the Nikolaev Line. Basaltic rocks from the ophiolites are dominantly E-MORB and minor N-MORB and T-MORB (Lomize et al. 1997). The overlapping of the ages of the Xiate T-MORB-type basalts and Terskey ophiolites as well as the tectonic interpretation strongly suggest that the former are the eastern extension of the Terskey ophiolitic belt. Consequently the Xiate MORB-type basalts are interpreted to be fragments of the Terskey ophiolites, which were probably formed at a mid-ocean spreading ridge environment. The Terskey ocean was likely to have been small in size, because it was relatively short-lived (Lomize et al. 1997) and studies on fauna assemblages indicate that the Yili and Tarim plates were intimately associated in the Cambrian (Guo 2001).

Voluminous volcanic arc magmatic rocks occur in the Terskey ophiolitic belt, ranging in age from early Cambrian to middle Ordovician (Lomize et al. 1997). For example, a granite from the western part of the Terskey ophiolitic belt is dated at 464.1 ± 1 Ma (Bazhenov et al. 2003), which is within the error identical to the crystallization age of the Xiate dioritic pluton. Thus, an arc setting is likely for the Xiate diorites, although a non-arc setting such as a continental collision regime cannot be ruled out.

Our data presented above substantiates the suggestions (Li and Li 1997; Li and Liu 1997) that the NNF is an extension of the Nikolaev Line. In addition, the data show that the Yili plate was separated from the Central Tianshan plate by the Terskey ocean in the early Paleozoic. The Terskey ocean is interpreted to have opened in late Neoproterozoic to early Cambrian and closed in the early stage of late Ordovician (Lomize et al. 1997). As a consequence, we consider that the NNF is an early Paleozoic suture zone, but not a secondary fault of the late Paleozoic STSZ.

Timescale of the STO

The tectonic evolution history of the STO is still poorly constrained. Generally, the STO is accepted to have been closed in early Carboniferous (Windley et al. 1990; Allen et al. 1992; Carroll et al. 1995; Gao et al. 1998, 2006). However, its opening was proposed to have occurred either in late Precambrian–early Paleozoic (Gao et al. 2006), Cambrian–Ordovician (Shi et al. 1994; Chen et al. 1999) or late Ordovician (Carroll et al. 1995; Gao et al. 1998). Ages of the ophiolitic, HP-LT metamorphic and arc rocks have been employed to define the timescale of the STO. Fossil data and recent Ar–Ar and SHRIMP dating results show

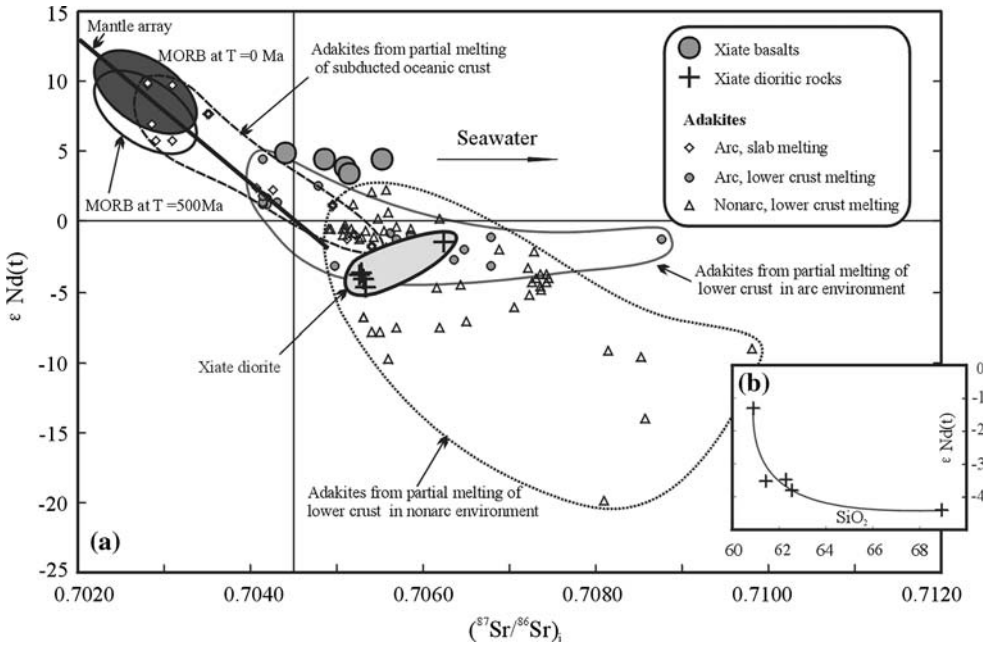

Fig. 12 εNd(t) versus $(^{87}Sr/^{86}Sr)_i$ diagram for samples from the Xiate basalts and dioritic pluton. *Filled and open ellipses* in top left-hand corner are fields of MORB at present (Ito et al. 1987) and at age of 500 Ma, respectively. The main correlation of young oceanic and selected continental basalts, namely the Mantle array (DePaolo and Wasserburg 1979), is shown assuming that the early Paleozoic mantle sources have a pattern similar to that of modern mantle sources (Jacobsen and Wasserburg 1979). The bulk silicate earth at present has $^{87}Sr/^{86}Sr$ of 0.7045 and $^{143}Nd/^{144}Nd$ of 0.512638 (εNd = 0). Phanerozoic adakites of different ages and tectonic environments are plotted for comparison. Data sources are: adakites from partial melting of subducted oceanic crusts—Kay et al. (1993), Stern and Kilian (1996) and Aguillón-Robles et al. (2001); adakites from partial melting of lower crust in arc environments—Muir et al. (1995) and Wareham et al. (1997); adakites from partial melting of lower crust in nonarc environments—Waight et al. (1998), Xu et al. (2002), van de Flierdt et al. (2003), Gao et al. (2004), Topuz et al. (2005) and Wang et al. (2005). *Horizontal arrow* shows effect of seawater alteration

that formation ages of the ophiolites from the South Tianshan fold belt and the arc-type magmatic rocks to the north side of the STSZ are confined in age from early Silurian to early Carboniferous (Gao et al. 1998, 2006, 2007; Jiang et al. 2001; Long et al. 2006; Zhu et al. 2006). The HP-LT metamorphic rocks display late Silurian–early Carboniferous peak metamorphic ages (Gao et al. 1995, 1998, 2000; Gao and Klemd 2003) and experienced late Carboniferous retrograde metamorphism (Klemd et al. 2005). These data show that the Chinese part of the STO was subducted to the north from early Silurian to early Carboniferous.

A late Neoproterozoic (single zircon Pb–Pb age, 590 ± 11 to 600 ± 15 Ma) mafic-ultramafic complex (the Dalubayi ophiolite) was recently reported in the HP-LT metamorphic rocks (Yang et al. 2005). Basalts and gabbros from this complex have enriched LREE contents and fractionated chondrite-normalized REE patterns, and were interpreted as ocean island magmatic rocks (Yang et al. 2005). However, the rocks have strong Ti and P depletion when compared to REE and their TiO_2 (0.82–0.90%) contents are considerably lower than that of typical ocean island basalts (Sun and McDonough 1989; Garcia et al. 2003 and references therein). Thus, it is more likely, that the complex formed in a continental rift environment as a result of the separation of the Tarim plate from the early Neoproterozoic Rodinia supercontinent, which started to split apart at about 820–750 Ma (Li et al. 2004). Up to now, no convincing evidence for the existence of a late Neoproterozoic–Ordovician ocean has been found along the Chinese part of the STSZ, although ophiolites and arc-type volcanics of similar ages have been reported in the South Tianshan fold belt to the west of the Talas-Fergana fault (Volkova and Budanov 1999; Brookfield 2000). Therefore, we adopt the suggestion of Carroll et al. (1995) and Gao et al. (1998) that the Chinese sector of the STO most likely started to open in late Ordovician.

A tectonic evolution model

The following model is proposed for the early Paleozoic tectonic evolution of the South Tianshan orogen in China (Fig. 15). From Sinian-early Cambrian to middle Ordovician, oceanic crust of the Terskey ocean separated the Yili plate from the Central Tianshan plate, the latter of which was probably connected with the Tarim plate (Fig. 15a). A thickened crust may have formed along the south margin of the Yili plate in early–middle Ordovician due to the subduction of the Terskey ocean. The Yili and Central

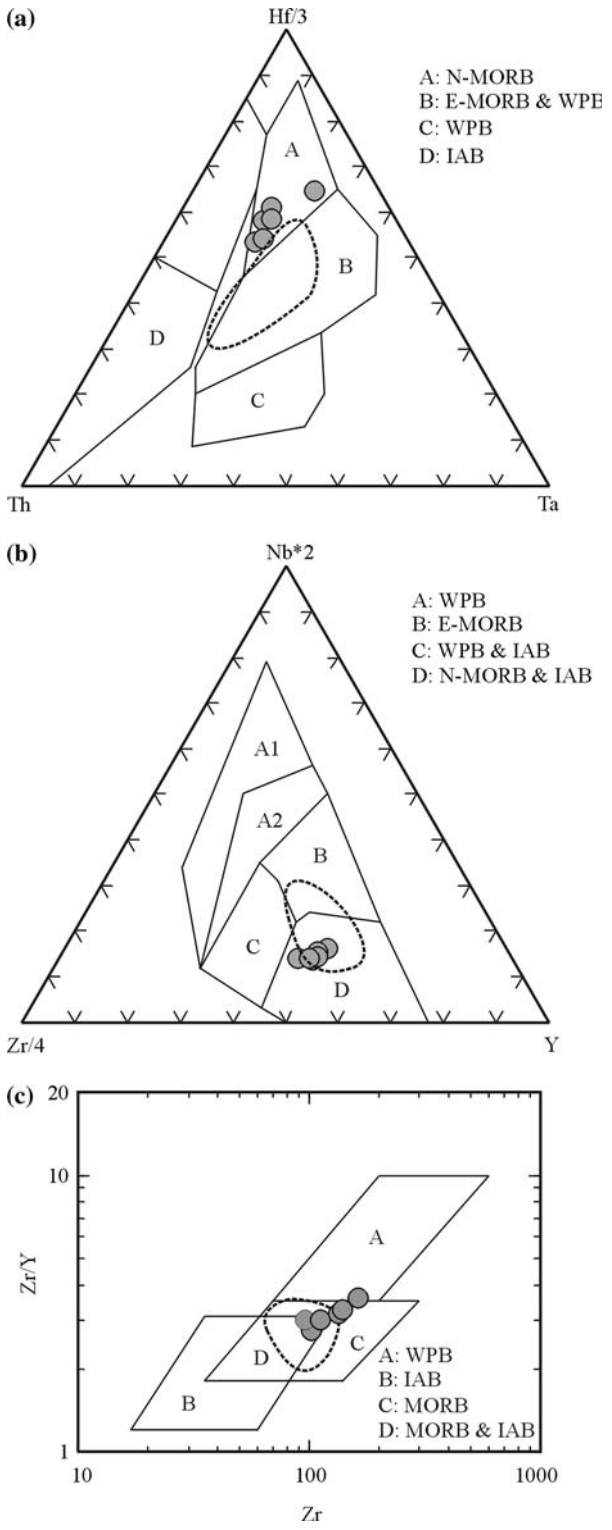

Fig. 13 Tectonic setting discrimination diagrams for the Xiate basalts. **a** Hf-Th-Ta diagram (Wood 1980), **b** Nb–Zr–Y diagram (Meschede 1986), **c** Zr/Y–Zr diagram (Pearce and Norry 1979). *Areas circled by dotted line* show compositions of transitional (T)-type MORB from the Red Sea axial trough (Altherr et al. 1988). *N-MORB* normal mid-ocean ridge basalt, *E-MORB* enriched mid-ocean ridge basalt, *IAB* island arc basalt, *WPB* within-plate basalt

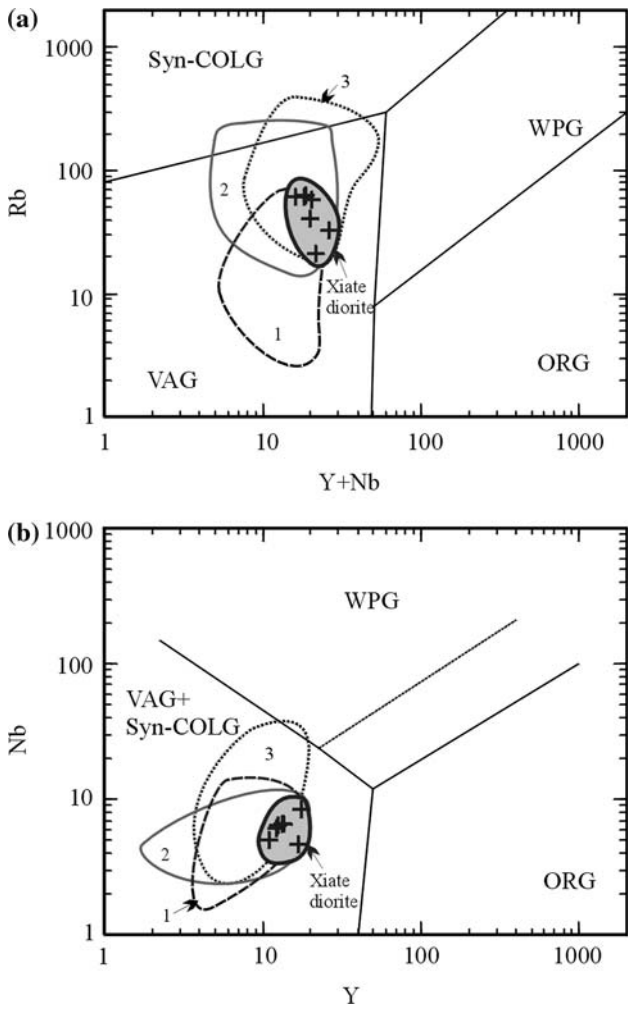

Fig. 14 Tectonic setting discrimination diagrams for the Xiate diorites (after Pearce et al. 1984). **a** Rb versus Y + Nb diagram; **b** Nb versus Y diagram. *ORG* ocean-ridge granites, *syn-COLG* syn-collisional granites, *VAG* volcanic arc granites, *WPG* within-plate granites. Areas labeled 1–3 are: *1* adakites from partial melting of subducted oceanic crusts; *2* adakites from partial melting of lower crust in arc environments; *3* adakites from partial melting of lower crust in nonarc environments. *Symbols* are the same as in Fig. 12

Tianshan plates collided in the early stage of late Ordovician due to the closure of the Terskey ocean (Lomize et al. 1997), which was followed by the opening of the STO (Fig. 15b). From early Silurian to early Carboniferous, the STO was subducted beneath the composite Yili–Central Tianshan plate (Fig. 15c), as was suggested by Gao et al. (1998).

Conclusions

Basalts from Xiate (South Tianshan, NW China) have a weighted mean $^{206}Pb/^{238}U$ formation age of 516.3 ± 7.4 Ma and a (T)-MORB and ferrobasaltic geochemistry, which was interpreted to most likely reflect a

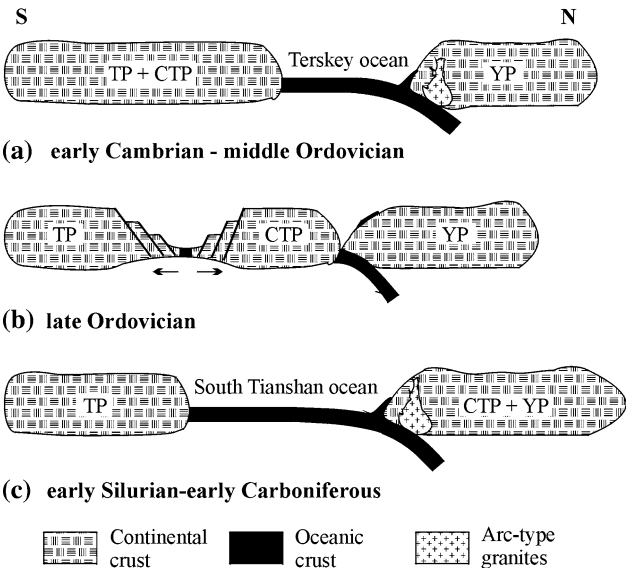

Fig. 15 A model for the early Paleozoic tectonic evolution of the Chinese Tianshan Orogen. *TP* Tarim plate, *CTP* Central Tianshan plate, *YP* Yili plate

propagating spreading center. The basalts were intruded by a dioritic pluton with a weighted mean $^{206}Pb/^{238}U$ crystallization age of 470 ± 12 Ma. The diorites have a calc-alkaline chemistry and major and trace elemental characteristics, which are typical of adakitic rocks. These geochemical as well as the Sr–Nd isotopic characteristics of the diorites indicate that they formed by partial melting of garnet amphibolites in a thickened crust in a volcanic arc or continental collision setting. The geochemical and SHRIMP U–Pb zircon data presented above provide the first evidence of Cambrian MORB-type basalts and Ordovician adakitic diorites, which occur between the Yili and Central Tianshan plates. Our data further substantiate that the Yili and Central Tianshan plates were separated by the Terskey ocean in early Paleozoic. The North Nalati fault is interpreted here for the first time as an early Paleozoic suture zone in the Chinese South Tianshan orogen.

Acknowledgments We are indebted to FK Chen, ZY Chu, CF Li, P Xiao and AL Zheng for help during the Sr–Nd isotopic analysis, and R Baur, JQ Wang, XD Jin and HY Li for help during the major and trace element analysis. H Tao and QD Zhang are acknowledged for handling the SHRIMP targets. XM Xiong and LL Long took part in the fieldwork. T. John's advices significantly improved the original manuscript. Two anonymous reviewers are highly appreciated for their constructive comments. This work was funded by the State Key Project for Basic Research of China (2007CB411302, 2001CB409803) and the National Natural Science Foundation of China (40672153, 40472047).

References

Aguillón-Robles A, Calmus T, Benoit M, Bellon H, Maury RC, Cotton J, Bourgois J, Michaud F (2001) Late Miocene adakites and Nb-enriched basalts from Vizcaino Peninsula, Mexico: indicators of East Pacific Rise subduction below southern Baja California? Geology 29:531–534

Allen MB, Windley BF, Zhang C (1992) Palaeozoic collisional tectonics and magmatism of the Chinese Tien Shan, central China. Tectonophysics 220:89–115

Altherr R, Henjes-Kunst F, Puchelt H, Baumann A (1988) Volcanic activity in the Red Sea axial trough-evidence for a large mantle diaper? Tectonophysics 150:121–133

Bazhenov ML, Collins AQ, Degtyarev KE, Levashova NM, Mikolaichuk AV, Pavlov VE, Van der Voo R (2003) Paleozoic northward drift of the North Tien Shan (Central Asia) as revealed by Ordovician and Carboniferous paleomagnetism. Tectonophysics 366:113–141

Bureau of Geological and Mineral Resources, Xinjiang provinces (BGXP) (1981) Hantengri geological and mineral map (K-44-XV). Urumqi, Xinjiang, scale 1:200,000

Black LP, Kamo SL, Allen CM, Aleinikoff JN, Davis DW, Korsch RJ, Roudoulis C (2003) TEMORA 1: a new zircon standard for Phanerozoic U–Pb geochronology. Chem Geol 200:155–170

Brookfield ME (2000) Geological development and Phanerozoic crustal accretion in the western segment of the southern Tien Shan (Kyrgyzstan, Uzbekistan and Tajikistan). Tectonophysics 328:1–14

Burtman VS, Skobelev SF, Molnar P (1996) Late Cenozoic slip on the Talas-Ferghana fault, the Tien Shan, central Asia. Geol Soc Am Bull 108:1004–1021

Carroll AR, Graham SA, Hendrix MS, Ying D, Zhou D (1995) Late Paleozoic tectonic amalgamation of northwestern China: sedimentary record of the northern Tarim, northwestern Turpan, and southern Junggar Basins. Geol Soc Am Bull 107:571–594

Che ZC, Liu HF, Liu L (1994) Formation and evolution of the middle Tianshan orogenic belt (in Chinese). Geological Publishing House, Beijing, pp 1–135

Chen CM, Lu HF, Jia D, Cai DS, Wu SM (1999) Closing history of the southern Tianshan oceanic basin, western China: an oblique collisional orogeny. Tectonophysics 302:23–40

Coleman RG (1989) Continental growth of northwest China. Tectonics 8:621–635

Condie KC (1997) Sources of Proterozoic mafic dyke swarms: constraints from Th/Ta and La/Yb ratios. Precamb Res 81:3–14

Debaille V, Blichert-Toft J, Agranier A, Doucelance R, Schiano P, Albarede F (2006) Geochemical component relationships in MORB from the mid-Atlantic Ridge, 22–35°N. Earth Planet Sci Lett 241:844–862

Defant MJ, Drummond MS (1990) Derivation of some modern arc magmas by melting of young subducted lithosphere. Nature 347:662–665

Defant MJ, Drummond MS (1993) Mount St. Helens: potential example of the partial melting of the subducted lithosphere in a volcanic arc. Geology 21:547–550

DePaolo DJ (1981) Neodymium isotopes in the Colorado Front Range and crust-mantle evolution in the Proterozoic. Nature 291:193–196

DePaolo DJ, Wasserburg GJ (1979) Petrogenetic mixing models and Nd–Sr isotopic patterns. Geochim Cosmochim Acta 43:615–627

Drummond MS, Defant MJ, Kepezhinskas PK (1996) Petrogenesis of slab-derived trondhjemite–tonalite–dacite/adakite magmas. Trans R Soc Edinburgh Earth Sci 87:205–215

Foley S, Tiepolo M, Vannucci R (2002) Growth of early continental crust controlled by melting of amphibolite in subduction zones. Nature 417:837–840

Gao J, Klemd R (2003) Formation of HP-LT rocks and their tectonic implications in the western Tianshan Orogen, NW China: geochemical and age constraints. Lithos 66:1–22

Gao J, He GQ, Li MS, Xiao XC, Tang YQ, Wang J, Zhao M (1995) The mineralogy, petrology, metamorphic PTDt trajectory and

exhumation mechanism of blueschists, south Tianshan, northwestern China. Tectonophysics 250:151–168
Gao J, Li MS, Xiao XC, Tang YQ, He GQ (1998) Paleozoic tectonic evolution of the Tianshan Orogen, northwestern China. Tectonophysics 287:213–231
Gao J, Zhang LF, Liu SW (2000) The $^{40}Ar/^{39}Ar$ age record of formation and uplift of the blueschists and eclogites in the western Tianshan Mountains. Chin Sci Bull 45:1047–1051
Gao S, Rudnick RL, Yuan HL, Liu XM, Liu YS, Xu WL, Ling WL, Ayers J, Wang XC, Wang QH (2004) Recycling lower continental crust in the north China craton. Nature 432:892–897
Gao J, Long LL, Qian Q, Huang DZ, Su W, Klemd R (2006) South Tianshan: a Late Paleozoic or a Triassic orogen?. Acta Petrol Sinica 22:1049–1061 (in Chinese with English abstract)
Gao J, John T, Klemd R, Xiong X (2007) Mobilisation of Ti-Nb-Ta during subduction: evidence from rutilebearing segregations and veins hosted in eclogites, Tianshan, NW China. Geochim Cosmochim Acta 71:4974–4996
Garcia MO, Pietruszka AJ, Rhodes JM (2003) A petrologic perspective of Kilauea volcano's summit magma reservoir. J Petrol 44:2313–2339
Guo FX (2001) Paleozoic tectono-paleobiogeography of Xinjiang, China. Xinjiang Geology 19:20–26 (in Chinese with English abstract)
Harper GD (2003) Fe–Ti basalts and propagating-rift tectonics in the Josephine Ophiolite. Geol Soc Am Bull 115:771–787
He GQ, Li MS (2000) New achievement in researching ophiolitic belts in central Asia and its significance in the links of tectonic belts between northern Xinjiang and adjacent area. Xinjiang Geology 18:193–202 (in Chinese with English abstract)
He GQ, Xu X (2004) The plate tectonic division of Chinese Tianshan: A consideration to Khazakhstan plate. In: He GQ, Xu X (eds) The collected papers on geology and minerals of Tianshan Mountain, Xinjiang area, China. Geological Publishing House, Beijing, pp 1–12 (in Chinese with English abstract)
He GQ, Li MS, Han BF (2001) Geotectonic research of southwest Tianshan and its west adjacent area, China. Xinjiang Geology 19:7–11 (in Chinese with English abstract)
Hendrix MS, Dumitru TA, Graham SA (1994) Late Oligocene–early Miocene unroofing in the Chinese Tian Shan: an early effect of the India–Asia collision. Geology 22:487–490
Ito E, White WM, Gopel C (1987) The O, Sr, Nd and Pb isotope geochemistry of MORB. Chem Geol 62:157–176
Jacobsen SB, Wasserburg GJ (1979) Nd and Sr isotopic study of the Bay of Islands ophiolite complex and the evolution of the source of midocean ridge basalts. J Geophys Res 84:7429–7445
Jiang CY, Wu WK, Li LC, Mu YM, Bai KY, Zhao XN (2001) Phanerozoic tectonic evolution of the eastern South Tianshan. Geological Publishing House, Beijing, pp 1–160 (in Chinese)
John T, Schenk V, Haase K, Scherer E, Tembo F (2003) Evidence for a Neoproterozoic ocean in south-central Africa from mid-oceanic-ridge-type geochemical signatures and pressure-temperature estimates of Zambian eclogites. Geology 31:243–246
Kay SM, Ramos VA, Marquez M (1993) Evidence in Cerro Pampa volcanic rocks for slab-melting prior to ridge-trench collision in southern South America. J Geol 101:703–714
Klemd R, Bröcker M, Hacker BR, Gao J, Gans P, Wemmer K (2005) New age constraints on the metamorphic evolution of the high-pressure/low-temperature belt in the western Tianshan Mountains, NW China. J Geol 113:157–168
Lameyre J, Bowden P (1982) Plutonic rock type series: discrimination of various granitoid series and related rocks. J Volcanol Geotherm Res 14:169–186
Le Roex AP, Dick HJB, Reid AM, Erlank AJ (1982) Ferrobasalts from the Spiess Ridge segment of the Southwest Indian Ridge. Earth Planet Sci Lett 60:437–451
Li XD, Li MS (1997) Tectonic correlation between the western Chinese Tianshan and its western adjacent area. Geol Rev 42:107–115 (in Chinese with English abstract)
Li XD, Liu JB (1997) Tectonic analysis of Laerdun Daban of west Tianshan Mountains, China. Xinjiang Geology 15:371–378 (in Chinese with English abstract)
Li ZX, Evans DAD, Zhang S (2004) A 90° spin on Rodinia: possible causal links between the Neoproterozoic supercontinent, superplume, true polar wander and low-latitude glaciation. Earth Planet Sci Lett 220:409–421
Lomize MG, Demina LI, Zarshchicov AV (1997) The Kyrgyz-Terskei paleoceanic basin in the Tien Shan. Geotectonics 31(6):463–482 (in Russian)
Long LL, Gao J, Xiong XM, Qian Q (2006) The geochemical characteristics and the age of the Kule Lake ophiolite in the southern Tianshan. Acta Petrol Sinica 22:65–73 (in Chinese with English abstract)
Maniar PD, Piccoli PM (1989) Tectonic discrimination of granitoids. Geol Soc Am Bull 101:635–643
Martin H, Smithies RH, Rapp R, Moyen JF, Champion D (2005) An overview of adakite, tonalite–trondhjemite–granodiorite (TTG), and sanukitoid: relationships and some implicatios for crustal evolution. Lithos 79:1–24
Meschede M (1986) A method of discrimination between different types of mid-ocean ridge basalts and continental tholeiites with the Nb–Zr–Y diagram. Chem Geol 56:207–218
Milanovsky EE (1996) Geology of Russia and adjacent domain. Publishing House of MGU, Moscow, pp 1–445 (in Russian)
Muir RJ, Weaver SD, Bradshaw JD, Eby GN, Evans JA (1995) The Cretaceous Separation Point batholith, New Zealand: granitoid magmas formed by melting of mafic lithosphere. J Geol Soc Lond 152:689–701
Pearce JA, Norry MJ (1979) Petrogenetic implications of Ti, Zr, Y, and Nb variations in volcanic rocks. Contrib Mineral Petrol 69:33–47
Pearce JA, Harris NB, Tindle AG (1984) Trace element discrimination diagrams for the tectonic interpretation of granitic rocks. J Petrol 25:956–983
Petford N, Atherton M (1996) Na-rich partial melts from newly underplated basaltic crust: the Cordillera Blanca Batholith, Peru. J Petrol 37:1491–1521
Petrini R, Joron JL, Ottonello G, Bonatti E, Seyler M (1988) Basaltic dykes from Zabargad Island, Red Sea: petrology and geochemistry. Tectonophysics 150:229–248
Pin C, Carme F (1987) A Sm–Nd isotopic study of 500 Ma old oceanic crust in the Variscan belt of Western Europe: the Chamrousse ophiolite complex, Western Alps (France). Contrib Mineral Petrol 96:406–413
Qian Q (2001) Adakite: geochemical characteristics and genesis. Acta Petrol Mineral 20:297–306 (in Chinese with English abstract)
Qian Q, Gao J, Xiong XM, Huang DZ, Long LL (2006) Petrogenesis and tectonic settings of Carboniferous volcanic rocks from north Zhaosu, western Tianshan Mountains: constraints from petrology and geochemistry. Acta Petrol Sinica 22:1307–1323 (in Chinese with English abstract)
Rapp RP, Watson EB (1995) Dehydration melting of metabasalt at 8–32 kbar: implications for continental growth and crust-mantle recycling. J Petrol 36:891–931
Rapp RP, Watson EB, Miller CF (1991) Partial melting of amphibolite/eclogite and the origin of Archean trondhjemite and tonalities. Precamb Res 51:1–25
Reynolds JR, Langmuir CH, Bender JF, Kastens KA, Ryan WBF (1992) Spatial and temporal variability in the geochemistry of basalts the East Pacific Rise. Nature 359:493–499
Rollinson HR (1993) Using geochemical data: evaluation, presentation, interpretation. Longmans, London, pp 1–352

Rudnick RL (1995) Making continental crust. Nature 378:571–578
Sen C, Dunn T (1994) Dehydration melting of a basaltic composition amphibolite at 1.5 and 2.0 GPa: implications for the origin of adakites. Contrib Mineral Petrol 117:394–409
Sengör AMC, Natal'in BA, Burtman VS (1993) Evolution of the Altaid tectonic collage and Palaeozoic crustal growth in Eurasia. Nature 364:299–307
Sheppard S, Griffin TJ, Tyler IM, Page RW (2001) High- and low-K granites and adakites at a Palaeoproterozoic plate boundary in northwestern Australia. J Geol Soc Lond 158:547–560
Shu LS, Yu JH, Charvet J, Laurent-Charvet S, Sang HQ, Zhang RG (2004) Geological, geochronological and geochemical features of granulites in the Eastern Tianshan, NW China. J Asian Earth Sci 24:25–41
Shi YS, Lu H, Jia D, Cai DS, Wu SM, Chen CM, Howell DG, Valin ZC (1994) Paleozoic plate-tectonic evolution of the Tarim and western Tianshan regions, western China. Int Geol Rev 36:1058–1066
Sinton JM, Wilson DS, Christie DM, Hey RN, Delaney JR (1983) Petrologic consequences of rift propagation on oceanic spreading ridges. Earth Planet Sci Lett 62:193–207
Sobel ER, Chen J, Heermance RV (2006) Late Oligocene–early Miocene initiation of shortening in the Southwestern Chinese Tianshan: implications for Neogene shortening rate variations. Earth Planet Sci Lett 247:70–81
Solomovich LI, Trifonov BA (2002) Postcollisional granites in the South Tien Shan Variscan collisional belt, Kyrguzstan. J Asian Earth Sci 21:7–21
Stern CR, Kilian R (1996) Role of the subducted slab, mantle wedge and continental crust in the generation of adakites from the Andean Austral volcanic zone. Contrib Mineral Petrol 123:263–281
Sun SS, McDonough WF (1989) Chemical and isotopic systematics of oceanic basalts: implications for mantle composition and processes. In: Saunders AD, Norry MJ (eds) Magmatism in the Ocean Basins, Geological Sociaty Special Publication, vol 42, pp 313–345
Sun SS, Nesbitt RW, SharaskinAY (1979) Geochemical characteristics of mid-ocean basalts. Earth Planet Sci Lett 44:119–138
Topuz G, Altherrr R, Schwarz WH, Siebel W, Satir M, Dokuz A (2005) Post-collisional plutonism with adakite-like signatures: the Eocene Saraycik granodiorite (Eastern Pontides, Turkey). Contrib Mineral Petrol 150:441–455
Van de Flierdt T, Hoernes S, Jung S, Masberg P, Hoffer E, Schaltegger U, Friedrichsen H (2003) Lower crustal melting and the role of open-system processes in the genesis of syn-orogenic quartz diorite-granite-leucogranite associations: constraints from Sr–Nd–O isotopes from the Bandombaai complex, Namibia. Lithos 67:205–226
Volkova NI, Budanov VI (1999) Geochemical discrimination of metabasalt rocks of the Fan-Karategin transitional blueschist/greenschist belt, South Tianshan, Tajikistan: seamount volcanism and accretionary tectonics. Lithos 47:201–216
Waight TE, Weaver SD, Muir RJ, Maas R, Eby GN (1998) The Hohonu batholith of North Westland, New Zealand: granitoid compositions controlled by source H2O contents and generated during tectonic transition. Contrib Mineral Petrol 130:225–239
Wang Q, McDermott F, Xu JF, Bellon H, Zhu YT (2005) Cenozoic K-rich adakitic volcanic rocks in the Hohxil area, northern Tibet: lower-crust melting in an intracontinental setting. Geology 33:465–468
Wang B, Shu LS, Cluzel D, Faure M, Charvet J (2006) Geochemical constraints on Carboniferous volcanic rocks of the Yili Block (Xinjiang, NW China): Implications for the tectonic evolution of Western Tianshan. J Asian Earth Sci (in press)
Wareham CD, Millar IL, Vaughan APM (1997) The generation of sodic granite magmas, western Palmer Land, Antarctic Peninsula. Contrib Mineral Petrol 128:81–96
Windley BF, Allen MB, Zhang C, Zhao ZY, Wang GR (1990) Paleozoic accretion and Cenozoic redeformation of the Chinese Tien Shan Range, central Asia. Geology 18:128–131
Wolf MB, Wyllie PJ (1994) Dehydration-melting of amphibolite at 10 kbar: the effect of temperature and time. Contrib Mineral Petrol 115:369–383
Wood DA (1980) The application of a Th-Hf-Ta diagram to problems of tectonomagmatic classification and to establishing the nature of crustal contamination of basaltic lavas of the British tertiary volcanic province. Earth Planet Sci Lett 50:11–30
Xu JF, Shinjo R, Defant MJ, Wang Q, Rapp RP (2002) Origin of Mesozoc adakitic intrusive rocks in the Ningzhen area of east China: partial melting of delaminated lower continental crust. Geology 30:1111–1114
Yang HB, Gao P, Li B, Zhang QJ (2005) The geological character of the Sinian Dalubayi ophiolite in the west Tianshan, Xinjiang. Xinjiang Geol 23:123–126 (in Chinese with English abstract)
Zhao ZH, Bai ZH, Xiong XL, Mei HJ, Wang YX (2003) $^{40}Ar/^{39}Ar$ chronological study of late Paleozoic volcanic-hypabyssal igneous rocks in western Tianshan, Xinjiang. Geochemica 32:317–327 (in Chinese with English abstract)
Zhu YF, Zhou J, Guo X (2006) Petrology and Sr-Nd isotopic geochemistry of the Carboniferous volcanic rocks in the western Tianshan Mountains, NW China. Acta Petrol Sinica 22:1041–1050 (in Chinese with English abstract)